Biophysical Journal
Article

Biophysical Society

Competitive Binding of Mg^{2+} and Na^{+} Ions to Nucleic Acids: From Helices to Tertiary Structures

Kun Xi,[1] Feng-Hua Wang,[2] Gui Xiong,[1] Zhong-Liang Zhang,[1] and Zhi-Jie Tan[1,*]
[1]Center for Theoretical Physics and Key Laboratory of Artificial Micro- and Nano-structures of Ministry of Education, School of Physics and Technology, Wuhan University, Wuhan, China and [2]Engineering Training Center, Jianghan University, Wuhan, China

ABSTRACT Nucleic acids generally reside in cellular aqueous solutions with mixed divalent/monovalent ions, and the competitive binding of divalent and monovalent ions is critical to the structures of nucleic acids because of their polyanionic nature. In this work, we first proposed a general and effective method for simulating a nucleic acid in mixed divalent/monovalent ion solutions with desired bulk ion concentrations via molecular dynamics (MD) simulations and investigated the competitive binding of Mg^{2+}/Na^{+} ions to various nucleic acids by all-atom MD simulations. The extensive MD-based examinations show that single MD simulations conducted using the proposed method can yield desired bulk divalent/monovalent ion concentrations for various nucleic acids, including RNA tertiary structures. Our comprehensive analyses show that the global binding of Mg^{2+}/Na^{+} to a nucleic acid is mainly dependent on its structure compactness, as well as Mg^{2+}/Na^{+} concentrations, rather than the specific structure of the nucleic acid. Specifically, the relative global binding of Mg^{2+} over Na^{+} is stronger for a nucleic acid with higher effective surface charge density and higher relative Mg^{2+}/Na^{+} concentrations. Furthermore, the local binding of Mg^{2+}/Na^{+} to a phosphate of a nucleic acid mainly depends on the local phosphate density in addition to Mg^{2+}/Na^{+} concentrations.

INTRODUCTION

Nucleic acids have important biological functions for genetic storage, expression, and regulation, and their functions are strongly coupled to their structures and structural changes (1,2). Since nucleic acids are highly charged polyanions, their native structure formation undergoes strong intramolecule Coulombic repulsions (1–26). However, metal ions in the solution can bind to nucleic acids and significantly reduce the Coulombic repulsion, thus favoring the structure folding of nucleic acids (1–11,13,23,25). Compared with monovalent ions, multivalent ions play a more important and efficient role in structure folding (e.g., Mg^{2+} of millimolar concentration can generally induce RNA folding), whereas Na^{+} can only cause RNA folding at approximately molar concentrations (8,9,12–36). More importantly, a nucleic acid generally resides in mixed divalent/monovalent ion solutions (1–7). Therefore, the competitive binding of divalent and monovalent ions is critical to the structure folding and stability of nucleic acids (8,9,12,32–45).

To understand ion-nucleic acid interactions, several classic polyelectrolyte theories have been developed and employed (15–22,35,46–58). The counterion condensation theory and the Poisson-Boltzmann (PB) theory have been successful in predicting various electrostatic properties of nucleic acids (20–22,46–58). However, the counterion condensation theory was developed for line-charge structure models at very dilute ion concentrations. Thus, it is inapplicable for nucleic acids with complex structures at finite salt concentrations (46,47). The PB theory ignores the ion-ion correlations and underestimates the role of multivalent ions in stabilizing nucleic acid structures (49–63) and helix assembly (53,64). The tightly bound ion (TBI) model has recently been developed to account for ion-ion correlation in binding to nucleic acids (52,53), and the model has been shown to improve predictions regarding the effect of Mg^{2+} in stabilizing RNA/DNA helices/hairpins and tertiary structures (52–54,61,62,64). However, the TBI model in its present version assumes all the atom charges are distributed in phosphate groups and thus would not result in reliable prediction of detailed ion binding properties in the vicinity of nucleic acids (54,62,64).

As an important complementary method to theories and experiments, all-atom molecular dynamics (MD) simulations can offer reliable predictions of the detailed ion-binding properties and dynamics of biomolecules (10,65–87). The binding of divalent or monovalent ions to double-stranded (ds) DNA or dsRNA in pure divalent or monovalent

Submitted October 16, 2017, and accepted for publication March 6, 2018.
*Correspondence: zjtan@whu.edu.cn
Kun Xi and Feng-Hua Wang contributed equally to this work.
Editor: Nathan Baker.
https://doi.org/10.1016/j.bpj.2018.03.001

ion solutions has been investigated extensively by all-atom MD simulations (27,28,66,72,74,75,82,85). Recently, all-atom MD simulations have been employed for dsDNA and dsRNA in mixed Mg^{2+}/Na^{+} solutions to investigate the competitive binding of Mg^{2+}/Na^{+} to dsDNA and dsRNA, and it has been shown that the competitive binding of Mg^{2+} and Na^{+} is strongly dependent on the relative divalent/monovalent ion concentration (27,28,66,82). However, these existing MD-based studies on the binding of divalent/monovalent ions generally involved dsDNA or dsRNA with a given length and seldom covered the competitive binding of divalent/monovalent ions for nucleic acid structures beyond the standard B-form and A-form helical structures (42,43,73,86,87), although the existing experiments indicate that the global binding of Mg^{2+}/Na^{+} (or K^{+}) can be strongly dependent on nucleic acid structures (1–6,10,63). Therefore, there is still a lack of comprehensive understanding on the competitive binding of divalent/monovalent ions, especially to various nucleic acid structures.

Furthermore, an important issue in simulating nucleic acids with arbitrary structures in mixed divalent/monovalent ion solutions via MD simulations is to efficiently simulate a nucleic acid solution with desired bulk divalent/monovalent ion concentrations so as to conveniently model experimental systems and analyze ion concentration effects (63,73,82,87). This is challenging, because the competitive binding of divalent/monovalent ions may be sensitive to the structures of nucleic acids as well as the relative divalent/monovalent ion concentrations, and an MD cell generally cannot become very large because of the extremely high computation cost. To simulate a 25-base-pair (bp) dsRNA in various mixed Mg^{2+}/Na^{+} solutions, Kirmizialtin and Elber employed a neutralization technique to partition Mg^{2+} and Na^{+} in their MD simulations, although the obtained bulk Mg^{2+}/Na^{+} concentrations deviated apparently from the desired concentrations (27,66). To simulate a 24-bp dsDNA in mixed Mg^{2+}/Na^{+} solutions via MD simulations, Yoo and Aksimetiev attempted to obtain the desired bulk Mg^{2+}/Na^{+} concentrations through adjusting ion numbers in their MD simulations and repeating the procedure, but the resultant bulk Mg^{2+}/Na^{+} concentrations still deviated visibly from the desired concentrations, and such treatment was obviously not efficient (82). To model S-adenosylmethionine (SAM-I) riboswitch in mixed Mg^{2+}/K^{+} solution via MD simulations, Hayes et al. also chose the numbers of ions in the MD cell through repeated MD trials to obtain the desired bulk Mg^{2+}/K^{+} concentrations (73). Therefore, it is still necessary to obtain a general and efficient method for simulating a nucleic acid with arbitrary structure in a mixed Mg^{2+}/Na^{+} solution with desired bulk ion concentrations.

In this work, we first proposed a general and efficient method for simulating a nucleic acid with arbitrary structure in a mixed Mg^{2+}/Na^{+} solution with desired bulk ion concentrations and examined the method through extensive MD simulations. Afterward, we investigated the competitive binding of Mg^{2+} and Na^{+} to extensive nucleic acids, including short dsDNA, dsRNAs, and several RNA tertiary structures. Our calculations were compared with available experimental data, and the global and local binding of Mg^{2+} and Na^{+} were analyzed in detail for various nucleic acids. The global binding of ions is characterized as the binding ions in excess of bulk ion concentration (27,28,66,82), and the local binding of ions is characterized by the closely binding of ions near phosphates. Our comprehensive analyses suggest the global binding of Mg^{2+} over Na^{+} to a nucleic acid is mainly dependent on the surface charge density and Mg^{2+}/Na^{+} concentrations, and the local binding of Mg^{2+} over Na^{+} to a phosphate of a nucleic acid depends mainly on the local phosphate density (i.e., the number of phosphates around a phosphate) in addition to Mg^{2+}/Na^{+} concentrations.

MATERIALS AND METHODS

Method for simulating a nucleic acid solution with desired bulk divalent/monovalent ion concentrations via MD simulations

Because the competitive binding of divalent/monovalent ions may be strongly dependent on many factors, such as divalent/monovalent ion concentrations and the length and structure of nucleic acids, it is challenging to propose a general and efficient method for simulating a nucleic acid in a mixed divalent/monovalent ion solution with desired bulk ion concentrations via MD simulations (27,66,73,82). The TBI model has been shown to successfully predict the global competitive binding between divalent/monovalent ions to various DNA and RNA structures (54). Through extensive TBI-based calculations for various DNA and RNA structures in mixed Mg^{2+}/Na^{+} solutions with wide range of Mg^{2+}/Na^{+} concentrations (54), an empirical equivalent formula between divalent and monovalent ions in neutralizing various nucleic acids has been derived (54):

$$\log\left[Na^{+}\right]_{Mg} = A\log\left[Mg^{2+}\right] + B, \tag{1}$$

where $[Na^{+}]_{Mg}$ and $[Mg^{2+}]$ are in millimolar and can achieve the equivalent ionic neutralization for a nucleic acid (54). The two parameters A and B in Eq. 1 are dependent on the length and compactness of a nucleic acid (54):

$$A = 0.65 + \frac{4.2}{N}\left(\frac{R_g}{R_g^0}\right)^2;\quad B = 1.80 - \frac{9.8}{N}\left(\frac{R_g}{R_g^0}\right)^2, \tag{2}$$

where N and R_g represent the number of phosphates and radius of gyration for a nucleic acid. R_g^0 is the radius of gyration for the A-form RNA helix with the same length N (–nt), which has been fitted to an empirical formula $R_g^0 = 0.406N + 130/(N + 11)$ (54). Based on Eq. 1, for a nucleic acid in a mixed Mg^{2+}/Na^{+} solution with desired bulk concentrations $[Mg^{2+}]$ and $[Na^{+}]$, the numbers N_{Mg}^c and N_{Na}^c of divalent/monovalent counterions for neutralizing the nucleic acid can be given by

$$N_{Mg}^c = N\frac{0.5[Na^{+}]_{Mg}}{[Na^{+}]_{Mg} + [Na^{+}]};\ N_{Na}^c = N\frac{[Na^{+}]}{[Na^{+}]_{Mg} + [Na^{+}]}, \tag{3}$$

respectively. Therefore, the total numbers for divalent/monovalent ions in the simulation cell are given by $N_{Mg}=N^c_{Mg}+N^s_{Mg}$ and $N_{Na}=N^c_{Na}+N^s_{Na}$, respectively. Here, N^s_{Mg} and N^s_{Na} are the numbers of divalent/monovalent ions dissociated from the added divalent/monovalent salts and can be calculated conveniently with the MD cell size and bulk salt concentrations ($[Mg^{2+}]$ and $[Na^+]$). Our simulation systems were kept neutral with addition of coions Cl^-.

All-atom MD simulations

In this work, we performed all-atom MD simulations in mixed Mg^{2+}/Na^+ solutions to 1) examine the method proposed above for simulating nucleic acids in mixed divalent/monovalent ion solutions with desired bulk divalent/monovalent ion concentrations; and 2) perform comprehensive analyses on the competitive binding of divalent/monovalent ions to diverse and representative constructs of nucleic acids (63,82). The nucleic acids used in our MD simulations include a 24-bp B-form dsDNA, an A-form dsRNA with different lengths (8-, 12-, and 24-bp), and four RNA tertiary structures: 28-nucleotide (nt) beet western yellow virus (BWYV) pseudoknot (Protein Data Bank (PDB): 437D) (88), 58-nt ribosomal RNA (rRNA) fragment (PDB: 1HC8) (89), 76-nt Yeast $tRNA^{Phe}$ (PDB: 1TRA) (90), and 94-nt SAM-I riboswitch (PDB: 2GIS) (91). The sequences of the dsDNA and dsRNAs are in Table S1. The initial structures of the dsDNA and dsRNA structures were built using the Nucleic Acid Builder of AMBER (AMBER Software, San Francisco, CA) (92), and the initial structures of RNA tertiary structures were taken directly from the PDB (93). The structures of the nucleic acids used in the work are shown in Fig. 1, and the nucleic acids, ion conditions, and the respective simulation cells are listed in Table 1. For the dsDNA and dsRNA structures, the simulation cells were chosen according to the previous simulational work (82) for the convenience of direct comparison, and for the RNA tertiary structures, the simulation cells were selected to ensure the distance between the edge of the cells and the surface of the RNA tertiary structures was larger than two times the Debye-Hückel length. All the details for the numbers of ions (Mg^{2+}, Na^+, and Cl^-) added in the simulation cells were listed in Table S2. In this work, Na^+ was chosen rather than K^+ according to the related experimental (63) and simulational works (27,28,66,73,82), although K^+ is more prevalent than Na^+ in intracellular environment.

In our MD simulations, the Amber parmbsc0 force field (92) was employed for DNA and RNA molecules in mixed Mg^{2+}/Na^+ ion solutions, combined with the TIP3P water model and Joung/Cheatham ion model for Na^+ and Cl^- (94) and Åqvist ion model for Mg^{2+} (95), in which ions were added by replacing the water molecules at least 20 Å away from the surface atom of nucleic acids, i.e., the atoms with the closest distance from the added ions. All the simulation systems were optimized, thermalized (298 K), and equilibrated with the program Gromacs 4.5 (96), with the periodic boundary conditions and particle mesh Ewald method for long-range interaction (97). All atoms in the nucleic acids were restrained by a harmonic potential with force constant 1000 kJ/mol·nm^{-2} in x-, y- and z-directions; hence, the effect of nucleic acid flexibility on ion binding was ignored. Each MD simulation was continued for 200 ns in the isothermic-isobaric ensemble (time step = 2 fs, P = 1 atm, and T = 298 K). Generally, our MD simulations for ion binding to various nucleic acids qualitatively nearly reach equilibrium after ~20 ns, as shown in Figs. S1 and S2. During all our simulations, the change on the box sizes is always less than 0.5 Å in each dimension, and it leads to a change of ~1.3% on the box volumes; thus, it would only have a slight effect on the calculated bulk ion concentrations. Additionally, we have examined the Mg^{2+} models of Allnér and Villa (98) and Li and Merz (99) for a 12-bp dsDNA (72) and did not find a significant

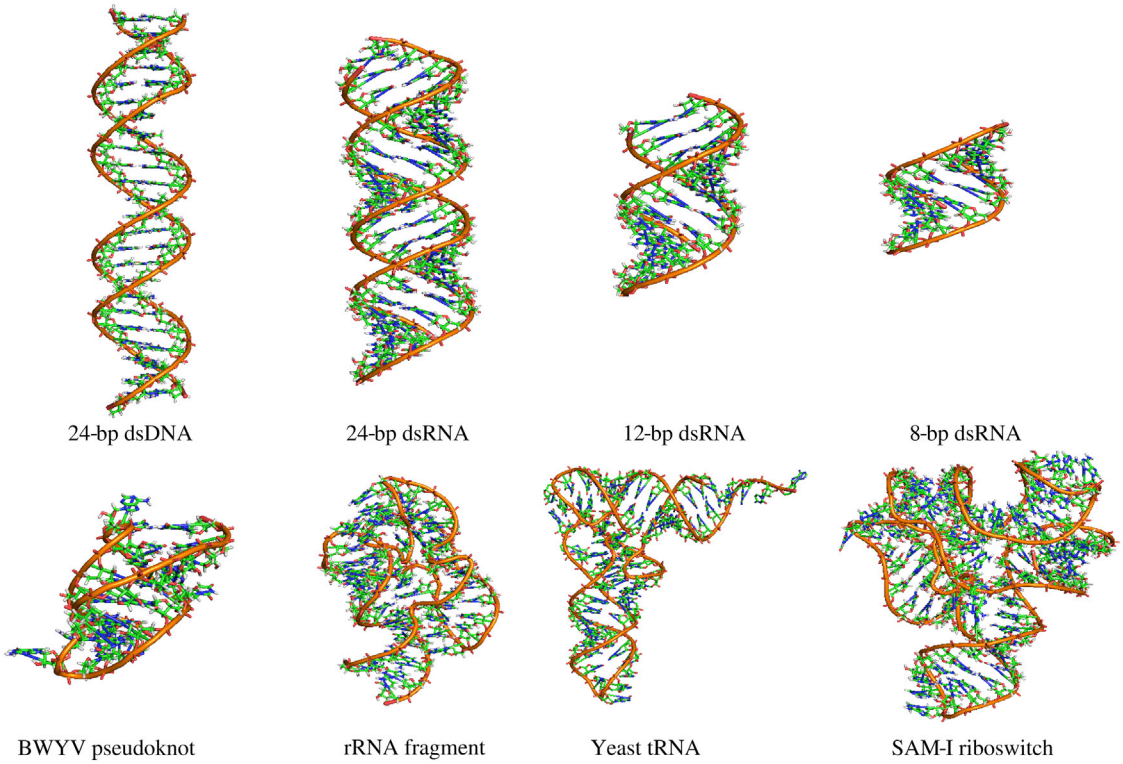

FIGURE 1 The DNA and RNAs used in our simulations, including 24-bp dsDNA; 24-bp, 12-bp, and 8-bp dsRNAs (63); BWYV pseudoknot (88); 58-nt rRNA fragment (89); yeast $tRNA^{Phe}$ (90); and SAM-I riboswitch (91). The structures for the nucleic acids are displayed with PyMol (http://www.pymol.org). To see this figure in color, go online.

TABLE 1 The DNA/RNA Molecules and the Respective MD Simulation Details in the Work

DNA or RNA	Desired Bulk $[Mg^{2+}]/[Na^+]$ (mM)	Cell Size (Å ^{3})	Simulation Time (ns)	Bulk $[Mg^{2+}]/[Na^+]$ in Reference[a] (mM)	Our Bulk $[Mg^{2+}]/[Na^+]$[b] (mM)
24-bp dsDNA	1/20	150 × 150 × 90	200	–	1.1 ± 0.1/20.2 ± 0.3
	5/20	150 × 150 × 90	200	7/18	5.4 ± 0.1/20.0 ± 0.2
	5/40	150 × 150 × 90	200	8/36	5.3 ± 0.1/40.4 ± 0.3
	5/70	150 × 150 × 90	200	8/72	5.2 ± 0.1/70.3 ± 0.2
	5/240	150 × 150 × 90	200	6/237	5.2 ± 0.2/241.6 ± 0.4
	5/420	150 × 150 × 90	200	7/418	5.3 ± 0.1/421.1 ± 0.3
	10/20	150 × 150 × 90	200	–	10.1 ± 0.1/20.8 ± 0.3
	20/20	150 × 150 × 90	200	–	20.9 ± 0.2/19.7 ± 0.2
	50/20	150 × 150 × 90	200	–	50.8 ± 0.7/20.7 ± 0.5
8-bp dsRNA	1/20	150 × 150 × 48	200	–	1.0 ± 0.1/21.5 ± 0.1
	10/20	150 × 150 × 48	200	–	10.9 ± 0.2/20.4 ± 0.2
12-bp dsRNA	1/20	150 × 150 × 58	200	–	1.0 ± 0.1/21.6 ± 0.8
	10/20	150 × 150 × 58	200	–	10.5 ± 0.3/19.7 ± 0.2
24-bp dsRNA	1/20	150 × 150 × 90	200	–	1.1 ± 0.1/20.2 ± 0.3
	5/20	150 × 150 × 90	200	–	5.1 ± 0.2/21.6 ± 0.3
	10/20	150 × 150 × 90	200	–	10.1 ± 0.1/21.6 ± 0.1
	50/20	150 × 150 × 90	200	–	50.8 ± 0.3/21.7 ± 0.1
28-nt BWYV Pseudoknot	1/20	120 × 110 × 110	200	–	1.0 ± 0.1/20.8 ± 0.2
	10/20	120 × 110 × 110	200	–	10.9 ± 0.2/20.5 ± 0.1
58-nt rRNA Fragment	1/20	130 × 130 × 120	200	–	1.1 ± 0.2/20.5 ± 0.1
	10/20	130 × 130 × 120	200	–	10.2 ± 0.2/19.5 ± 0.1
76-nt Yeast $tRNA^{Phe}$	1/20	130 × 145 × 160	200	–	1.1 ± 0.1/19.4 ± 0.3
	10/20	130 × 145 × 160	200	–	10.3 ± 0.1/19.1 ± 0.1
94-nt SAM-I Riboswitch	1/20	120 × 145 × 140	200	–	1.0 ± 0.1/21.0 ± 0.2
	10/20	120 × 145 × 140	200	–	10.1 ± 0.1/20.5 ± 0.1

In the table, the sequences of dsDNA and dsRNAs are listed in Table S1, and BWYV pseudoknot, rRNA fragment, Yeast $tRNA^{Phe}$, and SAM-I riboswitch represent a 28-nt beet western yellow virus (BWYV) pseudoknot fragment (PDB: 437D) (88), a 58-nt ribosomal RNA fragment (PDB: 1HC8) (89), 76-nt Yeast $tRNA^{Phe}$ (PDB: 1TRA) (90), and 94-nt S-adenosylmethionine riboswitch mRNA (PDB: 2GIS) (91), respectively.

[a]The bulk $[Mg^{2+}]/[Na^+]$ values are obtained from Yoo and Aksimetiev (82).

[b]The bulk $[Mg^{2+}]/[Na^+]$ values are obtained from our MD simulations.

effect of Mg^{2+} models on the Mg^{2+} distribution around the 12-bp dsDNA; see Fig. S3. We have also performed additional simulations for 24-bp dsDNA and 58-nt rRNA fragment in 1 mM Mg^{2+}/20 mM Na^+ solution with different initial positions of ions.

The Poisson-Boltzmann calculations

In addition to the all-atom simulations described above, we also calculated the binding ions in excess of bulk ions and the surface electrostatic potentials for various nucleic acids with the PB theory (52–54,59,60). For calculating the binding ions in excess of bulk ions to nucleic acids, we used the three-dimensional finite-difference algorithm developed in the TBI model for our convenience (52). A three-step focusing process was employed, and the resolutions for the three steps were kept as 2.0, 1.0, and 0.5 Å per grid respectively. The grid size (L_x, L_y, L_z) of the first, second, and third runs were kept larger than 10, 6, and 2 times the Debye-Hückel length from the surface of a nucleic acid and varied with different DNA and RNA molecules. Other details about the solvent have been described in (52,54). For calculating the surface electrostatic potential for nucleic acids, we used the APBS software (49), since the obtained surface potential can be conveniently displayed with VMD (100). In all the PB calculations, the dielectric constant inside nucleic acids was set to be two, and that of solvent was taken as 78.5. The radii of Mg^{2+} and Na^+ were taken as 3.0 Å (101) and 2.0 Å (102), respectively.

RESULTS AND DISCUSSION

First, we have examined the proposed method for efficiently simulating a nucleic acid in mixed divalent/monovalent solutions with desired bulk ion concentrations via MD simulations. Second, we have performed a detailed comparative analysis on the binding of Mg^{2+} and Na^+ to dsDNA and dsRNA. Third, we have focused on the binding of Mg^{2+} and Na^+ to various RNA tertiary structures with different lengths and compactness. Finally, we have summarized what governs the global and local binding of Mg^{2+} and Na^+ to various nucleic acid structures. In addition, our calculations are compared with the available experimental data and cover the wide ranges of ion concentrations and nucleic acid structures. In our analyses, we will use the binding ions in excess of bulk ions to characterize the global binding of ions to nucleic acids (37,54) and use detailed ion distributions and closely binding ions near phosphates to characterize the local binding of ions to various nucleic acids.

Simulating a nucleic acid in mixed Mg^{2+}/Na^+ solutions with desired bulk ion concentrations

As described in the Materials and Methods, we proposed a method aiming to efficiently model the system of a nucleic acid in mixed Mg^{2+}/Na^+ solutions with desired bulk ion concentrations via MD simulations. In the following, we have examined whether a one-time MD run with the use

of the proposed method can yield the desired bulk ion concentrations for various RNA/DNA molecules in extensively mixed Mg^{2+}/Na^{+} conditions. The ion concentration $c_\alpha(r)$ around a nucleic acid can be calculated by

$$c_\alpha(r) = \frac{N_\alpha(r+dr) - N_\alpha(r)}{V(r+dr) - V(r)}, \quad (4)$$

where $V(r)$ and $N_\alpha(r)$ denote the volume and the number of ions within a distance r from the nucleic acid, respectively, and α stands for ion species. For dsDNA and dsRNA helices, r is the radial distance from the helical axis that was obtained with the program of Curves+ (103), $V(r)$ stands for the cylinder volume within r without excluding DNA or RNA volume, and $c_\alpha(r)$ was previously used to analyze ion distribution around dsDNA/dsRNA (19,20,26,74,95). For RNA tertiary structures in which an axis cannot be well defined, r stands for the distance from the surface atoms (the atoms with closest distance from the examined ions), and $V(r)$ excludes the volume of the RNAs. According to Eq. 4, the bulk ion concentrations can be obtained at large r, as shown in Figs. S4–S6. In the following, we have examined the obtained bulk divalent/monovalent ion concentrations for various nucleic acids in comparison with the desired concentrations.

For dsDNA and dsRNA of different lengths, we made extensive examinations on bulk ion concentrations over the wide range of $[Mg^{2+}]$ and $[Na^{+}]$. As shown in Table 1, our proposed method can yield the bulk $[Mg^{2+}]$ and $[Na^{+}]$, which are very close to the desired values. The mean relative deviations of $[Mg^{2+}]$ and $[Na^{+}]$ from the desired ones are ~5 and ~4%, respectively. Here, the mean relative deviation of $[Mg^{2+}]$ is slightly larger than that of $[Na^{+}]$ because the desired bulk $[Mg^{2+}]$ is generally lower (~mM) than the desired bulk $[Na^{+}]$. Although the largest relative deviation of $[Mg^{2+}]$ comes from a mixed solution of 1 mM Mg^{2+} and 20 mM Na^{+}, the absolute deviation of $[Mg^{2+}]$ is only ~0.1 mM. Compared with the previous work (e.g., (82)), our obtained bulk $[Mg^{2+}]$ and $[Na^{+}]$ are much closer to the desired values (e.g., the mean relative deviations of $[Mg^{2+}]$ from our MD and (82) for the total cases are ~5 and ~44%, respectively), given the same simulation cell (82) (see Table 1). Additionally, our method is much more efficient because only one MD run is required for each case with the proposed method described in the Materials and Methods.

For various RNA tertiary structures ranging from 28-nt BWYV pseudoknot to 94-nt SAM-I riboswitch, the obtained bulk $[Mg^{2+}]/[Na^{+}]$ in our MD simulations are all close to the desired values, as shown in Table 1. The mean relative deviations of $[Mg^{2+}]$ and $[Na^{+}]$ from the desired values are rather small (~5% for $[Mg^{2+}]$ and ~4% for $[Na^{+}]$). In a recent MD simulation of SAM-I riboswitch in mixed Mg^{2+}/K^{+} solution, Hayes et al. obtained the desired bulk ion concentrations with the slightly larger mean relative deviations of Mg^{2+} (~5.1% for $[Mg^{2+}]$) by repeating several MD trials (73), in which the slightly smaller mean relative deviation of $[K^{+}]$ (~2%) may be caused by the high desired bulk concentration (~100 mM) (73). It should be noted that our proposed method only requires one MD run even for various RNA tertiary structures (see the Materials and Methods) to yield desired bulk ion concentrations for simulating various RNA tertiary structures in mixed Mg^{2+}/Na^{+} solutions, although larger RNA tertiary structures (>94 nt) have not been examined here.

Therefore, the above extensive examinations show that our proposed method is effective and efficient for simulating a nucleic acid with arbitrary structure in mixed divalent/monovalent ion solutions with wide ranges of desired bulk ion concentrations. It is encouraging that only a single MD simulation is required for a nucleic acid in a mixed Mg^{2+}/Na^{+} solution to yield the desired bulk Mg^{2+}/Na^{+} concentrations, and the method is expected to work for other mixed divalent/monovalent ion solutions such as mixed Mg^{2+}/K^{+} solutions.

Competitive binding of Mg^{2+}/Na^{+} to duplexes: dsDNA versus dsRNA

Global binding of Mg^{2+}/Na^{+} and comparison with experiments

Since the global binding of ions is directly coupled to the global stability of nucleic acids (1–9,36–38), we calculated the number of global binding ions for both dsDNA and dsRNA (27,28,66). According to (27,28,66,72,82), the numbers N_α^b of global binding ions of species α in excess of bulk ion concentrations can be calculated as those ions:

$$N_\alpha^b = \int_0^\infty \left(c_\alpha(r) - c_\alpha^0\right) d^3r. \quad (5)$$

Based on the ion concentration distributions and the bulk ion concentrations c_α^0 shown in Table 1 and Figs. S5 and S6, the numbers N_{Mg}^b, N_{Na}^b, and N_{Cl}^b of global binding $Mg^{2+}/Na^{+}/Cl^{-}$ around the 24-bp dsDNA or dsRNA were calculated through Eq. 5.

As shown in Fig. 2, *A* and *B* and in Table S2, for both dsDNA and dsRNA, with the increase of $[Mg^{2+}]$ from 1 to 50 mM, N_{Mg}^b increases apparently and N_{Na}^b decreases simultaneously, suggesting the anticooperative binding between Mg^{2+} and Na^{+}. Since the number of negative charges on a nucleic acid is unchanged, the increase of N_{Mg}^b (or N_{Na}^b) causes the decrease of N_{Na}^b (or N_{Mg}^b). Fig. 2, *A* and *B* also show that N_{Mg}^b for dsRNA is always slightly larger than that for dsDNA over the range of $[Mg^{2+}]$ from 1 to 50 mM, and correspondingly, N_{Na}^b for dsRNA is slightly smaller than that for dsDNA. The larger number N_{Mg}^b for dsRNA than for dsDNA can be attributed to the more

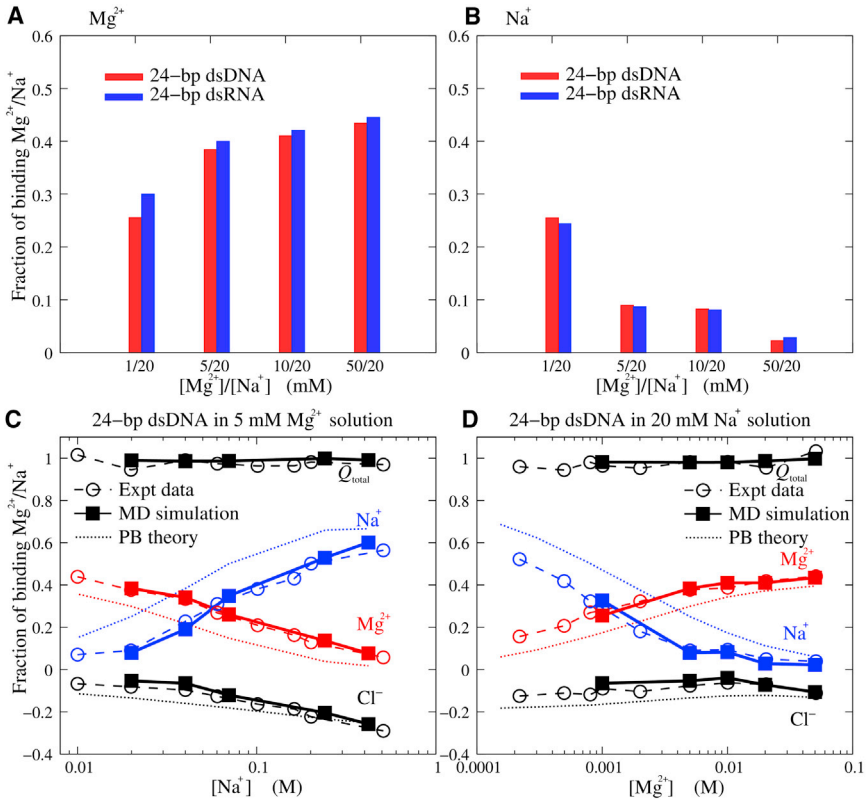

FIGURE 2 (*A* and *B*) The fractions of binding Mg^{2+} (*A*) and Na^{+} (*B*) per nucleotide around the 24-bp dsDNA and dsRNA. (*C* and *D*) These panels show the fractions of binding Mg^{2+}, Na^{+}, and Cl^{-} per nucleotide and the total charge fraction Q_{total} of the ion atmosphere (Mg^{2+}, Na^{+}, and Cl^{-}) for the 24-bp dsDNA as functions of $[Na^{+}]$ (*C*) and $[Mg^{2+}]$ (*D*). Dashed lines with circles represent experimental data (63); solid lines with squares represent MD simulations; and dotted lines represent PB theory. To see this figure in color, go online.

compact structure of dsRNA: A-RNA is slightly shorter than B-DNA, which results in higher charge density and stronger Mg^{2+} binding for dsRNA.

Fig. 2, *C* and *D* show the experimental data (63), our MD calculations, and the PB calculations for N^b_{Mg} and N^b_{Na} around the 24-bp dsDNA. First, the total charge fraction Q_{total} of binding ions (Mg^{2+}, Na^{+}, and Cl^{-}) almost keeps unity, suggesting that the systems are neutral. Second, N^b_{Mg} (or N^b_{Na}) increases with the increase of $[Mg^{2+}]$ (or $[Na^{+}]$), and the increase (decrease) of N^b_{Mg} is generally accompanied with the decrease (increase) of N^b_{Na}. As discussed above, increased ion (Mg^{2+} or Na^{+}) concentration reduces the entropic penalty for ion binding and consequently favors the ion (Mg^{2+} or Na^{+}) binding, and the interplay between N^b_{Mg} and N^b_{Na} is attributed to the unchanged number of negative charges on a nucleic acid. Third, our MD calculations are in accordance with the experimental data for N^b_{Mg}, N^b_{Na}, and N^b_{Cl} (55), suggesting that all-atom MD simulations can capture the ion-binding properties despite the computation cost. Fourth, the PB theory apparently underestimates N^b_{Mg} and correspondingly overestimates N^b_{Na}, although it predicts the trend of ion binding with ion concentration. Physically, the PB theory assumes the mean fluid-like ion distribution and consequently ignores the discrete properties of ions such as ion correlations, which would allow ions to self-organize to low-energy states and favor the binding of multivalent ions (52–54,61,62). Thus, the PB theory underestimates Mg^{2+} binding and overestimates Na^{+} binding. The systematic deviations of the PB theory were also observed previously in the Monte Carlo simulations and PB calculations for polymeric DNA in mixed salt solutions (20). Our additional calculations show the influence of the choice of dielectric constant of nucleic acids and radii of Mg^{2+} and Na^{+} for the PB results on the numbers of binding ions; see Fig. S7.

Mg^{2+}/Na^{+} distributions around duplexes: B-DNA versus A-RNA

Beyond the above-described global binding, we performed analyses on Mg^{2+}/Na^{+} distributions around dsDNA and dsRNA. As shown in Fig. 3, the radial concentration distributions of Mg^{2+} and Na^{+} around dsDNA and dsRNA share the following similar features: 1) there are two major peaks in the radial distributions of Mg^{2+} at two radial locations, and the height of the peaks increases with the increase of bulk $[Mg^{2+}]$; and 2) the radial distribution of Na^{+} appears much lower than that of Mg^{2+} and decreases for higher bulk $[Mg^{2+}]$. The higher peaks of Mg^{2+} and lower peaks of Na^{+} for higher $[Mg^{2+}]$ are due to the lowered binding entropy penalty of Mg^{2+}, and the overall lower radial concentration of Na^{+} than Mg^{2+} is attributed to the higher charge of Mg^{2+} and the corresponding stronger binding of Mg^{2+}. The two major peak locations of Mg^{2+} suggest the two different Mg^{2+} binding modes for dsDNA and dsRNA.

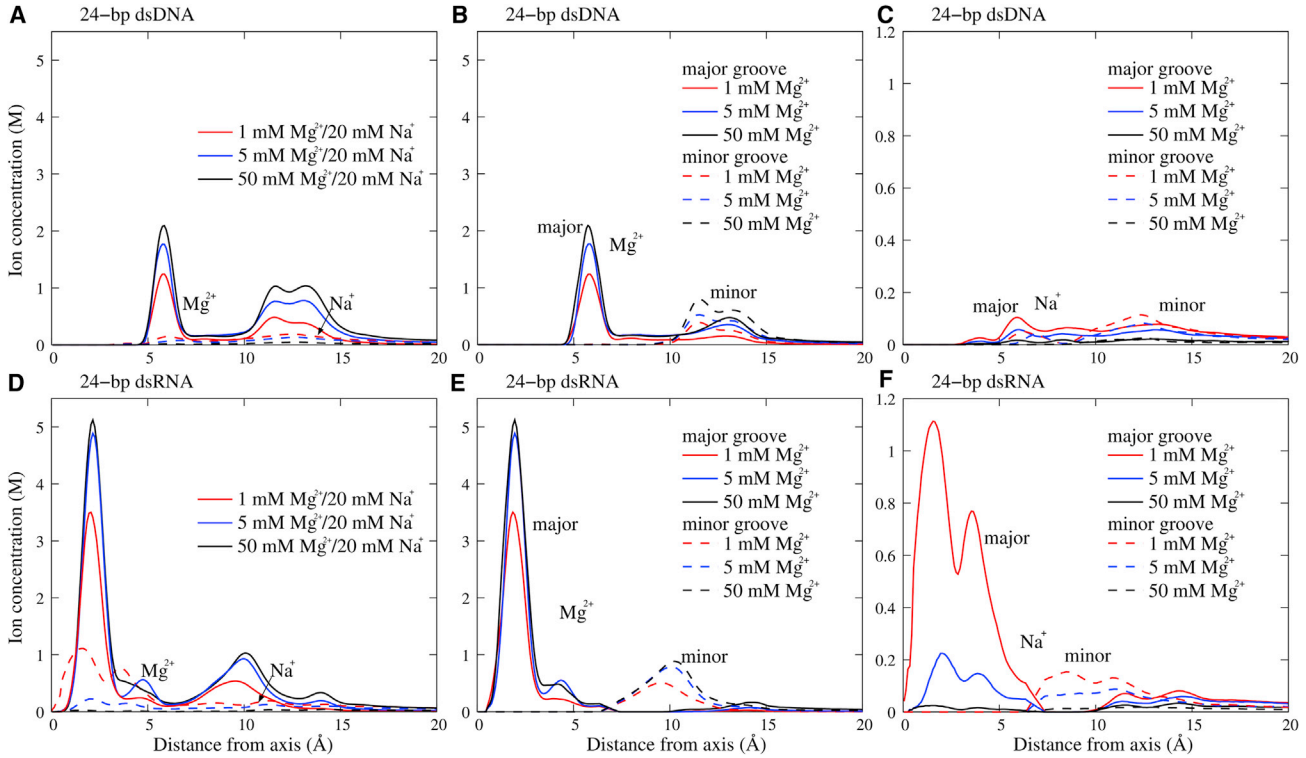

FIGURE 3 (*A* and *D*) The radial concentration distributions of Mg^{2+} and Na^{+} around 24-bp dsDNA (*A*) and dsRNA (*D*) in 20 mM Na^{+} solutions with different [Mg^{2+}] values. (*B* and *E*) These panels show the Mg^{2+} concentration distributions in/above the minor groove (*dashed lines*) and the major groove (*solid lines*) for the 24-bp dsDNA (*B*) and dsRNA (*E*). (*C* and *F*) These panels show the Na^{+} concentration distributions in/above the minor groove (*dashed lines*) and the major groove (*solid lines*) for the 24-bp dsDNA (*C*) and dsRNA (*F*). To see this figure in color, go online.

The detailed comparison between dsDNA and dsRNA also shows a distinctive difference in ion binding (e.g., Mg^{2+}): the radial locations for two major peaks are apparently different (~6 and ~12.5 Å for dsDNA, and ~2 and ~10 Å for dsRNA), and the heights of the first peaks of Mg^{2+} and Na^{+} (near-radial distance of ~2 Å) for dsRNA are much higher than those for dsDNA (near-radial distance of ~6 Å). To understand this difference, we divided the radial concentration distributions of Mg^{2+} and Na^{+} into those in (or over) major and minor grooves for dsDNA and dsRNA. As shown in Fig. 3, *B* and *C*, for dsDNA, Mg^{2+} can bind into the major groove at a radial distance of ~6 Å, whereas Mg^{2+} can bind more deeply and strongly into the major groove of dsRNA at a radial distance of ~2 Å. The next preferred binding of Mg^{2+} is above the minor groove (at a radial distance of ~12.5 Å) for dsDNA, and between phosphate strands in the minor groove (at a radial distance of ~10 Å) for dsRNA. Na^{+} can also bind more deeply and strongly into the major groove of dsRNA than to dsDNA, although the radial concentration of Na^{+} is much lower than that of Mg^{2+} because of the lower ionic charge, as shown in Fig. 3, *E* and *F*. The apparent difference in Mg^{2+} binding between dsDNA and dsRNA is attributed to their different helical structures: A-form dsRNA has a much deeper/narrower major groove and a wider minor groove than B-form dsDNA, which causes very different surface electrostatic potentials for dsDNA and dsRNA (see Figs. 1 and 4). Accordingly, we illustrated the spatial concentration distributions of Mg^{2+} and Na^{+} around dsDNA and dsRNA at different bulk Mg^{2+}/Na^{+} concentrations. As shown in Fig. 4, for dsRNA, the deep and narrow major groove is the most preferred binding domain for both Mg^{2+} and Na^{+}, and Mg^{2+} binding to the minor groove can become visible at high bulk [Mg^{2+}] because the narrow major groove can be almost fulfilled by Mg^{2+}. However, for dsDNA, the binding to the major groove and minor groove are both visible, whereas this appears weaker than the binding to the major groove of dsRNA. As [Mg^{2+}] increases, Mg^{2+} binding to major and minor grooves becomes stronger for both dsDNA and dsRNA, and simultaneously, Na^{+} binding becomes weaker. Our additional simulations with different initial positions of ions and with longer cell size in the *z* axis for 24-bp dsDNA yielded similar bulk ion concentrations and ion distributions; see Fig. S8. Additionally, we observed more binding Mg^{2+} ions in the GGG region of the major groove of the 24-bp dsDNA because the guanine bases can hold Mg^{2+} ions more strongly (74); see Fig. S9.

The different ion binding modes for dsDNA and dsRNA have been suggested to be responsible for the different multivalent ion-dependent condensation behaviors (27,28,34,66,73,82) and flexibilities for dsDNA and dsRNA (64,65).

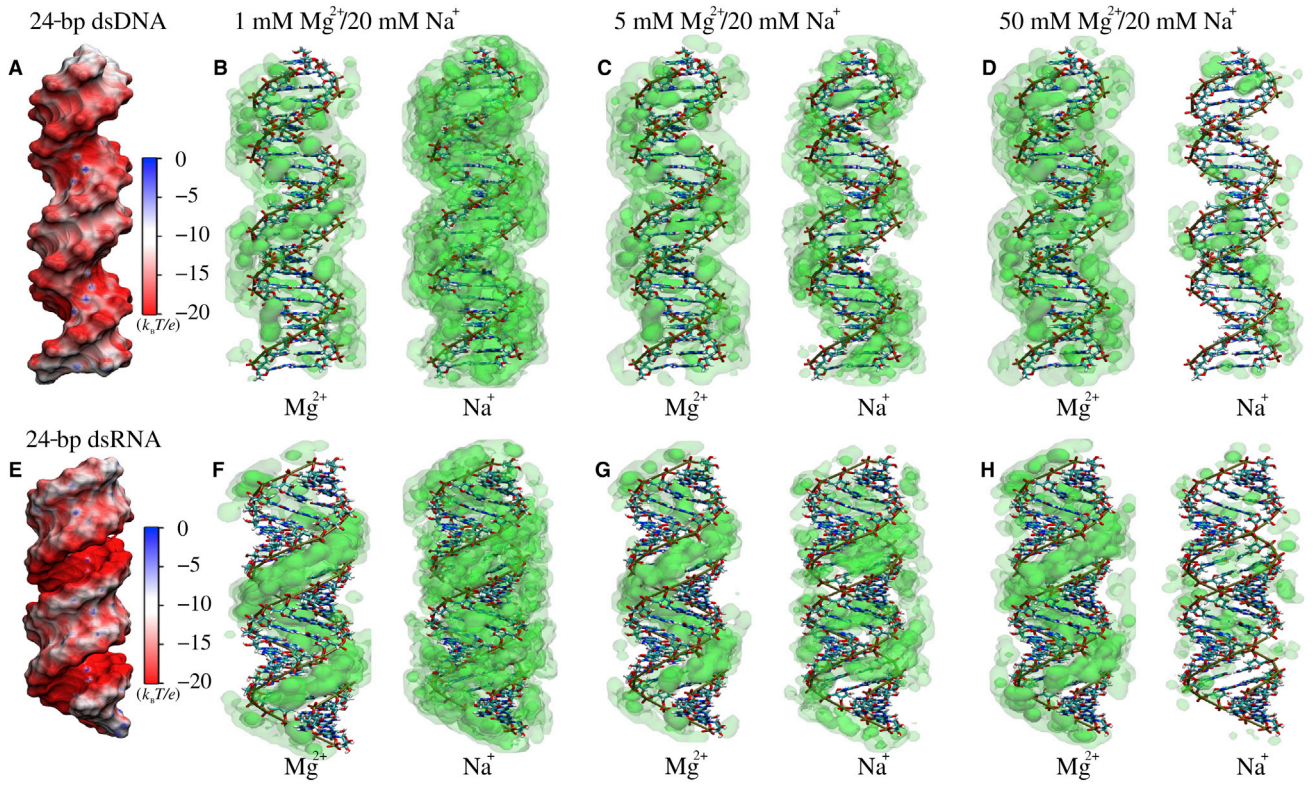

FIGURE 4 (*A* and *E*) The electrostatic potentials at the Mg^{2+} accessible surface of the 24-bp dsDNA (*A*) and dsRNA (*E*) were calculated by APBS (49). Shown is the electrostatic potential computed 3 Å away (the radius of hydrated Mg^{2+} is ~3 Å (80)) from the surface by VMD (100). (*B–D* and *F–H*) The spatial ion concentration distributions of Mg^{2+} and Na^{+} around the surface of 24-bp dsDNA and dsRNA are displayed in green of three-level opacities (0.5 M–5 M, 5 M–10 M, and >10 M for Mg^{2+} and 0.25 M–0.5 M, 0.5 M–2.0 M, and >2.0 M for Na^{+}, respectively) by VMD (100). To see this figure in color, go online.

Competitive binding of Mg^{2+}/Na^{+} to RNA tertiary structures

Beyond dsDNA and dsRNA helices, we analyzed the competitive binding of Mg^{2+} and Na^{+} to various RNA tertiary structures, including 28-nt BWYV pseudoknot, 58-nt rRNA fragment, 76-nt Yeast $tRNA^{Phe}$, and 94-nt SAM-I riboswitch.

Global binding of Mg^{2+} and Na^{+} to RNA tertiary structures

Since numbers of binding Mg^{2+}/Na^{+} are associated with the global stability of RNA tertiary structures, we calculated the numbers (N_{Mg}^{b} and N_{Na}^{b}) of binding Mg^{2+}/Na^{+} to various RNA tertiary structures as those in excess of bulk ion concentrations according to Eq. 5. As shown in Fig. 5, *A* and *B* and in Table S2, N_{Mg}^{b} and N_{Na}^{b} from the MD simulations are in accordance with those from the empirical formula from the TBI model, which has been quantitatively tested by the extensive experimental data for various RNA tertiary structures (54). Fig. 5, *A* and *B* also show that for higher bulk [Mg^{2+}], N_{Mg}^{b} increases and N_{Na}^{b} simultaneously decreases because of the lower entropy penalty of Mg^{2+} at higher [Mg^{2+}]. Furthermore, compared with the predictions from the MD simulations and the TBI model, the PB theory significantly underestimates N_{Mg}^{b} and simultaneously overestimates N_{Na}^{b}. As described above, this is because the PB theory ignores the ion correlation and fluctuation that allow ions to self-organize to low-energy states and favor multivalent ion binding (52–54,61,62).

For different RNA tertiary structures, N_{Mg}^{b} exhibits the following order: 94-nt SAM-I riboswitch > 58-nt rRNA fragment > 76-nt Yeast $tRNA^{Phe}$ > 28-nt BWYV pseudoknot. If we include the DNA/RNA helices, the order of N_{Mg}^{b} is as follows: 94-nt SAM-I riboswitch > 58-nt rRNA fragment > 76-nt Yeast $tRNA^{Phe}$ > 24-bp dsRNA > 28-nt BWYV pseudoknot > 24-bp dsDNA > 12-bp dsRNA > 8-bp dsRNA, and N_{Na}^{b} follows the reversal order. This indicates that the global competitive binding of Mg^{2+}/Na^{+} to RNAs may depend not only on RNA length but also structure compactness, and global Mg^{2+} binding appears stronger for RNAs with longer length and more compact structures.

Mg^{2+}/Na^{+} distributions around RNA tertiary structures

Beyond the analyses described above on the global binding of Mg^{2+} and Na^{+}, we have performed analyses on the detailed binding of Mg^{2+} and Na^{+} to various RNA tertiary

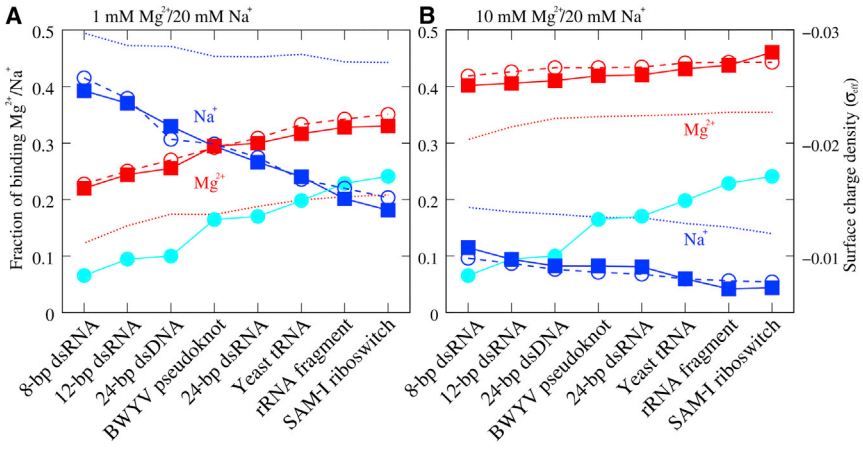

FIGURE 5 The number fractions of binding Mg^{2+} and Na^{+} per nucleotide for various RNA/DNA molecules in mixed 1 mM Mg^{2+}/20 mM Na^{+} (*A*) and 10 mM Mg^{2+}/20 mM Na^{+} (*B*) ion solutions. Solid lines with squares represent MD simulations; dotted lines represent PB theory; dashed lines with circles represent TBI predictions (Eq. 5 in (54)); and solid lines with spheres represent the effective surface charge density σ_{eff}. Here, RNA/DNA molecules were listed according to the order of fraction of binding Mg^{2+}/Na^{+}. The effective surface charge density (in units of $e/Å^2$) was calculated through considering an RNA/DNA as an ellipsoid; see the Supporting Material. To see this figure in color, go online.

structures, including the BWYV pseudoknot, rRNA fragment, yeast $tRNA^{Phe}$, and SAM-I riboswitch.

Since RNA tertiary structures are generally more complex than DNA/RNA duplexes and there is no well-defined axis, we calculated the ion concentrations $c(r)$ from the surface atoms of the RNA tertiary structures according to Eq. 4. As shown in Fig. 6, the concentration distributions of Mg^{2+} and Na^{+} share a similar trend for various RNA tertiary structures: 1) the location of the peaks of Mg^{2+} is ~4 Å, and the peak heights of Mg^{2+} are apparently higher than those of Na^{+}; and 2) with the increase of $[Mg^{2+}]$, the peak height of Mg^{2+} increases, and correspondingly, that of Na^{+} decreases. The location of ~4 Å from surface atoms suggests that Mg^{2+} keeps its hydrated shell in binding to various RNAs because of the very high dehydration penalty for Mg^{2+} (33–35,66), and it is hard for Mg^{2+} to become dehydrated within finite MD simulation time (72,81). However, monovalent ions can become partially dehydrated in binding to RNAs because of the much lower dehydration energy (71–73). The stronger Mg^{2+} binding and lower Na^{+} binding at higher bulk $[Mg^{2+}]$ is attributed to the lowered penalty for Mg^{2+} binding and the anticooperative binding between Mg^{2+} and Na^{+}. Despite the above described similarity in ion binding, the peak heights of Mg^{2+} distributions appear different for various RNA tertiary structures and follow the same order as that of N_{Mg}^{b}: 94-nt SAM-I riboswitch > 58-nt rRNA fragment > 76-nt Yeast $tRNA^{Phe}$ > 28-nt BWYV pseudoknot; see Fig. 5, *A* and *B*. This order nearly follows the same order of RNA length except for the 58-nt rRNA fragment, which appears relatively more compact than $tRNA^{Phe}$ and BWYV pseudoknot (54,62). This also suggests that Mg^{2+} binding to RNA tertiary structures may be dependent on not only RNA length but also its structural compactness. Compared to Mg^{2+} binding, the difference in Na^{+} binding between different RNA tertiary structures appears relatively slight because of the strong Mg^{2+} binding.

To further reveal the detailed binding of Mg^{2+}/Na^{+} to RNA tertiary structures, we have illustrated the surface electrostatic potentials and spatial concentration distributions in Fig. 7. Although the detailed binding of Mg^{2+}/Na^{+} exhibits specific patterns for different RNA tertiary structures, the detailed binding of Mg^{2+} and Na^{+} to various RNA tertiary structures share the following similar features: 1) Mg^{2+} prefers to bind deeply into the major groove of A-form helical stems and the junction pocket between helical stems even at

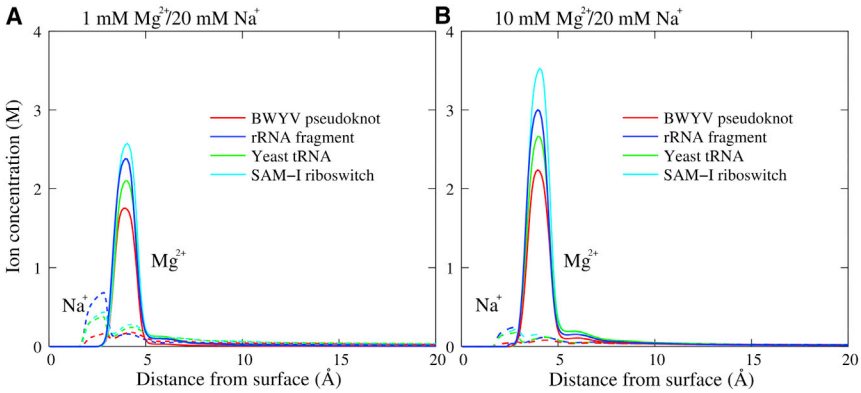

FIGURE 6 The ion concentration distributions of Mg^{2+} and Na^{+} around various RNA tertiary structures in mixed 1 mM Mg^{2+}/20 mM Na^{+} (*A*) and 10 mM Mg^{2+}/20 mM Na^{+} (*B*) solutions. The RNA tertiary structures include BWYV pseudoknot (*red*), 58-nt rRNA fragment (*blue*), yeast $tRNA^{Phe}$ (*green*), and SAM-I riboswitch (*cyan*), and distance from surface denotes that from surface atoms. To see this figure in color, go online.

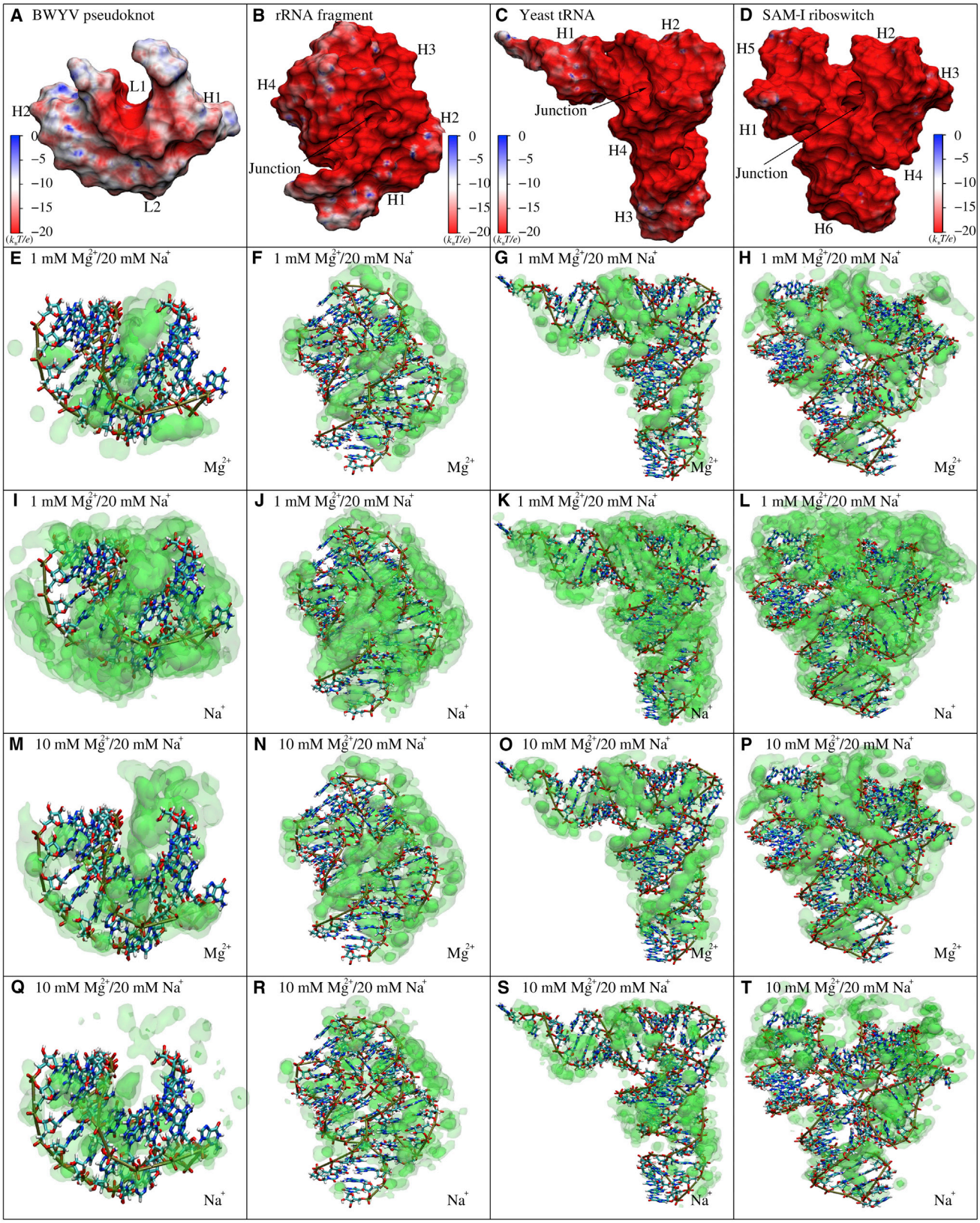

FIGURE 7 (*A–D*) The electrostatic potentials at the Mg^{2+} accessible surface of BWYV pseudoknot (*A*), 58-nt rRNA fragment (*B*), yeast $tRNA^{Phe}$ (*C*), and SAM-I riboswitch (*D*) were calculated by APBS (49). Shown is the electrostatic potential computed 3 Å away (the radius of hydrated Mg^{2+} is ~3 Å (80)) from the surface by VMD (100). (*E–T*) The spatial ion concentration of Mg^{2+} and Na^+ around BWYV pseudoknot (*E*, *I*, *M*, and *Q*), 58-nt rRNA fragment

(legend continued on next page)

low [Mg^{2+}]; 2) the binding of Na^+ into major grooves of helical elements/junction pocket is overwhelmed by Mg^{2+} binding, and Na^+ prefers to bind relatively loosely around RNA tertiary structures; and 3) the increase of [Mg^{2+}] causes more pronounced Mg^{2+} binding in both of the binding locations (to major groove/junction). These features for different RNA tertiary structures are understandable. As shown in Fig. 7 and Fig. S11, there is visible coupling between the local concentration distribution of Mg^{2+} and the local surface electrostatic potential. The surface potential is very negative in major grooves of helical stems and the junction pocket, and these sites are favorable for Mg^{2+} binding rather than Na^+ binding because of the higher charge of Mg^{2+}. Na^+ can only bind loosely to RNAs because of low ionic charge. The increase of [Mg^{2+}] decreases the entropy penalty of Mg^{2+} binding, which would enhance Mg^{2+} binding and more strongly suppress Na^+ binding. It is noted that the binding of Mg^{2+} to a multibranched junction may be essential in stabilizing specific RNA tertiary structures (1,5–10,12,37–39,42–44,73,86,87).

What governs the binding of Mg^{2+} and Na^+ to a nucleic acid?

The global and local binding of Mg^{2+} and Na^+ to various nucleic acids has been analyzed and discussed extensively. However, the question remains as to whether there is a simple rule that governs the competitive binding of Mg^{2+} and Na^+ to different nucleic acid structures in addition to Mg^{2+}/Na^+ concentrations. Therefore, in this study, we have attempted to explore such a rule for global binding of Mg^{2+}/Na^+ to various nucleic acid structures. We also attempted to explore the rule for the local binding of Mg^{2+}/Na^+ to various RNA tertiary structures. Here, our analyses cover both ds nucleic acids and RNA tertiary structures to understand the general rule for competitive binding of Mg^{2+}/Na^+, although the binding of Mg^{2+} and a variety of other cationic ligands binding to single-stranded and ds nucleic acids has been reported and discussed previously (6,15–23).

Global binding of Mg^{2+}/Na^+ to nucleic acid structures

According to the above analyses, the global binding of Mg^{2+}/Na^+ mainly depends on the length and the compactness of RNA/DNA structures. We investigated whether there is a simple parameter related to RNA/DNA structure for quantifying the global binding of Mg^{2+}/Na^+. Since surface charge density has been previously shown to be a determining parameter for ion binding to spherical and cylindrical polyelectrolytes (47,48), we calculated the surface charge densities for various RNA/DNA structures (47,48). Since the surface charge density cannot be clearly defined for a nucleic acid with complex structure, we can approximately model a nucleic acid as an ellipsoid, and the surface charge density σ_{eff} of the nucleic acid can be estimated as that of the ellipsoid (see the Supporting Material for details).

As shown in Fig. 5, *A* and *B*, with the increase of the effective surface charge density σ_{eff} for various RNA/DNA molecules, the number N_{Mg}^b of binding Mg^{2+} increases monotonously and that of Na^+ (N_{Na}^b) decreases monotonously in both 1 mM Mg^{2+}/20 mM Na^+ and 10 mM Mg^{2+}/20 mM Na^+ solutions. Such correlations between N_{Mg}^b (and N_{Na}^b) and σ_{eff} are interesting and reasonable. Physically, Mg^{2+} (Na^+) binding would become more pronounced (weaker) to a nucleic acid with higher surface charge density because Mg^{2+} with higher ionic charge interacts more strongly with a nucleic acid. Therefore, we propose that the effective surface charge density σ_{eff} mainly governs the global binding of Mg^{2+}/Na^+ to various nucleic acids, including RNA tertiary structures, in addition to Mg^{2+}/Na^+ concentrations. It is noted that our results in Figs. 5 and S12 are also consistent with the experimental analyses of the interactions of Mg^{2+} and Na^+ with nucleic acids and the effects of mixtures of these ions on protein-DNA binding (15,16). Our further analyses suggest that length N may also affect the global binding of Mg^{2+}/Na^+ when nucleic acids are not large, and an empirical linear coupling between the fraction of binding Mg^{2+}/Na^+ and $(1 - 3/N)\sigma_{\text{eff}}$ has been found for all the nucleic acids we used, as shown in Fig. S12. This Coulombic effect and $1/N$ dependence of ion accumulation/binding have been previously observed for nucleic acid oligomers in a series of PB- and Monte Carlo-based theoretical studies (17–19,21–23).

Local binding of Mg^{2+}/Na^+ to RNA tertiary structures

Beyond the global binding to a nucleic acid, what governs the local binding of Mg^{2+}/Na^+ to the nucleic acid? Here, we will use the closely binding of ions near phosphates to characterize the local binding of Mg^{2+}/Na^+.

Because the negative charges of a nucleic acid converge on phosphate groups and the local binding of Mg^{2+}/Na^+ is generally around phosphates, we will examine the local competitive binding of Mg^{2+}/Na^+ to phosphates for various RNA tertiary structures. First, we calculated the local phosphate density (i.e., local number N_p of phosphates around a phosphate) within a distance of ~9 Å, which was taken according to the phosphate-phosphate radial distribution function for various RNA tertiary structures in Fig. S13 *A*. According to the different number of N_p centered at all phosphates, the phosphates of RNA tertiary structures can

(*F*, *J*, *N*, and *R*), yeast $tRNA^{Phe}$ (*G*, *K*, *O*, and *S*), and SAM-I riboswitch (*H*, *L*, *P*, and *T*) are displayed in green of three-level opacities (0.5 M–5 M, 5 M–10 M, and >10 M for Mg^{2+} and 0.25 M–0.5 M, 0.5 M–2.0 M, and >2.0 M for Na^+, respectively) by the VMD (100). In panels (*A–D*), the names of helical stems, loops, and junctions correspond to those in the secondary structures in Fig. S10. The view of the panels in the opposite direction can be found in Fig. S11. To see this figure in color, go online.

be classified into several groups, and the larger N_p represents the more compact domain with higher local charge density as shown in Fig. 8 *A*. Simultaneously, the fractions f_{Mg}/f_{Na} of closely binding Mg^{2+}/Na^+ to phosphates were obtained by calculating the numbers of Mg^{2+}/Na^+ within a small distance around the phosphate atoms, and the small distance was chosen according to the phosphate-Mg^{2+} radial distribution function in Fig. S13 *B*. The distributions of N_p and f_{Mg} along phosphate strands for various RNA tertiary structures are shown in Fig. S14, and there is visible correlation between N_p and f_{Mg} for respective phosphates. Furthermore, we calculated the average number fractions of closely binding Mg^{2+}/Na^+ per phosphate for different N_p. As shown in Fig. 8, *B* and *C* and in Table S3, we found that the average number fraction of closely binding Mg^{2+} ($\overline{f}_{Mg}$) increases apparently with the increase of the local phosphate density N_p and becomes saturated at high N_p. Such an increment is more pronounced, and the saturated value of $\overline{f}_{Mg}$ is larger for higher [Mg^{2+}]. In contrast, the increase of the fraction of closely binding Na^+ with N_p is weak and appears visible at low (~1 mM) [Mg^{2+}]. This is because the higher charge of Mg^{2+} causes more sensitive binding of Mg^{2+} to the increased local charge density (N_p) of RNAs than that of Na^+. The increase of [Mg^{2+}] enhances the close binding of Mg^{2+} and weakens the close binding of Na^+ because of the lowered binding entropy penalty and the anticooperative binding between Mg^{2+} and Na^+. The saturation of $\overline{f}_{Mg}$ at large N_p may be attributed to the reduced Mg^{2+}-accessible space around a phosphate with the increase of N_p for the phosphate. Our additional simulation with different initial ion positions for 58-nt rRNA fragment shows a similar ion concentration distributions and local binding of ions; see Fig. S16. Additionally, our simulation for 28-nt BWYV pseudoknot without constraint does not show a significant effect of RNA flexibility on bulk ion concentrations and local binding of ions; see Fig. S17. It is interesting that the average number fractions of closely binding Mg^{2+} as functions of N_p converge for different RNA tertiary structures. This is understandable. The local close binding of Mg^{2+}/Na^+ near a site may be mainly dependent on the local charge density around the site rather than the whole RNA structure because ion binding/screening would diminish the electrostatic potential from other phosphates of RNAs beyond the vicinity of the binding site.

CONCLUSIONS

In this study, we performed all-atom MD simulations for various nucleic acids including dsDNA, dsRNA, and several RNA tertiary structures. A simple and efficient method for partitioning divalent/monovalent ions to simulate a nucleic acid system with desired divalent/monovalent bulk ion concentrations was proposed and validated for extensive nucleic acids in mixed Mg^{2+}/Na^+ solutions. The global binding and local binding of Mg^{2+} and Na^+ were analyzed for various nucleic acids including several RNA tertiary structures, and our calculations are in accordance with the available experimental data. Through extensive calculations and analyses, we have obtained the following major conclusions:

1) We have proposed a simple and efficient method for partitioning divalent/monovalent ions to simulate a nucleic acid in mixed divalent/monovalent ion solutions, and only one MD simulation is required for a nucleic acid with arbitrary structure in a mixed Mg^{2+}/Na^+ solution to obtain desired bulk divalent/monovalent ion concentrations. The method has been tested and validated for extensive nucleic acids and a wide range of mixed divalent/monovalent ion conditions.

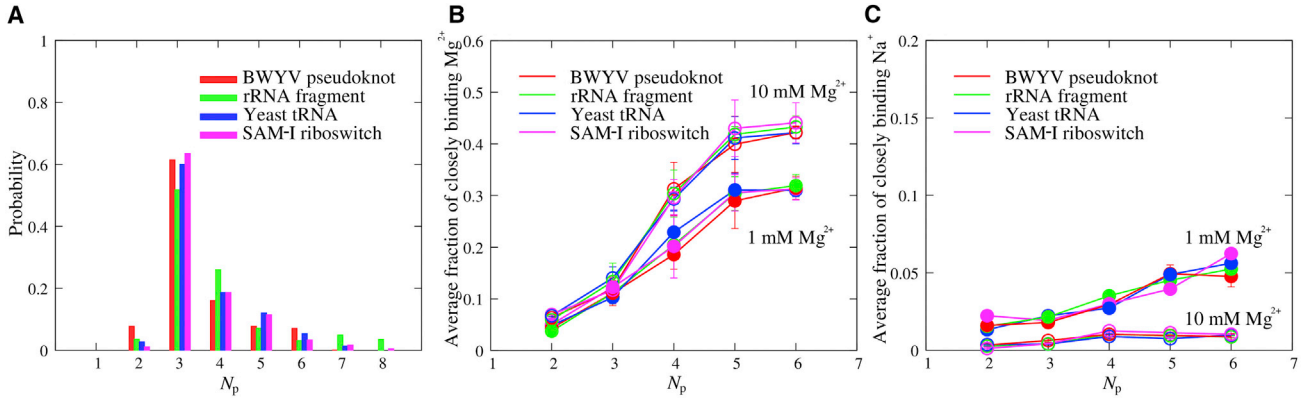

FIGURE 8 (*A*) The normalized distribution probability of the local phosphate density N_p for various RNA tertiary structures; N_p for a phosphate denotes the number of phosphates within a distance of 9 Å around the phosphate. (*B* and *C*) These show the average number of closely binding Mg^{2+} (*B*) and Na^+ (*C*) around phosphates within a distance of 5 Å for RNA tertiary structures in 1 mM Mg^{2+}/20 mM Na^+ and 10 mM Mg^{2+}/20 mM Na^+ solutions, respectively. The cutoff distances for N_p and for closely binding Mg^{2+}/Na^+ were selected according to the radial distributions of phosphates and Mg^{2+} around phosphates (see Fig. S13). The change of cutoff distance from 5 to 6 Å for phosphate-Mg^{2+} does not significantly change the curves of average fractions of closely binding Mg^{2+} and N_p (see Fig. S15). To see this figure in color, go online.

2) The global binding of Mg^{2+} (Na^{+}) to dsRNA is slightly stronger (weaker) than that to dsDNA, and Mg^{2+} binding is much more pronounced than Na^{+} binding for both dsRNA and dsDNA. Furthermore, Mg^{2+} binding to dsRNA is more likely to occur in the deep groove than that to dsDNA. Such difference is attributed to the different helical structures: A-form dsRNA is shorter and has deeper/narrower major grooves and wider/shallower minor grooves in comparison with B-form dsDNA.
3) The global binding of Mg^{2+}/Na^{+} to RNA tertiary structures depends on the structure compactness and chain length in addition to Mg^{2+}/Na^{+} concentrations. Through comprehensive analyses, we found the apparent correlation between global binding of Mg^{2+}/Na^{+} and the effective surface charge density for various nucleic acid molecules.
4) Local binding of Mg^{2+}/Na^{+} near the RNA surface is dependent on the local structures around binding sites, and favorable binding sites are generally in the major grooves of stems and junctions. The local binding of Mg^{2+}/Na^{+} near a phosphate is found to be visibly correlated to the local phosphate density for various RNA tertiary structures.

Although our proposed partition formula works very well for extensive nucleic acids over the wide range of mixed divalent/monovalent ion conditions, and our predictions agree well with the available experimental data, there are still some simplifications and limitations in our work. First, we employed the Åqvist force field for Mg^{2+} (95) rather than other Mg^{2+} models (81,98,99), such as the NBFIX hydrated Mg^{2+} model (81). However, this treatment should not significantly affect our major analyses and conclusions because previous simulations have shown that Mg^{2+} ions generally become hydrated before accumulating near nucleic acids, and the majority of Mg^{2+} ions would generally keep their hydrated shell (72,86). The minority of possible chelated Mg^{2+} ions would be somewhat related to the adopted force fields for Mg^{2+} (86). Second, our MD simulations did not cover the salt concentrations below 1 mM [Mg^{2+}], since too-low salt concentrations would make the simulation cell too large and bring a huge computation cost. Finally, in our MD simulations, all the nucleic acids are restrained with a strong harmonic potential, and we consequently ignored the effect of flexibility of nucleic acids on ion binding. The interplay of flexibility and ion binding for RNA tertiary structures is an important issue and deserves to be discussed elsewhere. Nevertheless, this work proposed a simple and useful method for simulating a nucleic acid solution with desired mixed divalent/monovalent ion concentrations, and our analyses and results will be helpful for understanding the binding of divalent/monovalent ion to extensive DNAs and RNAs.

SUPPORTING MATERIAL

Supporting Materials and Methods, seventeen figures, and three tables are available at http://www.biophysj.org/biophysj/supplemental/S0006-3495(18)30297-2.

AUTHOR CONTRIBUTIONS

Z.-J.T., K.X., and F.-H.W. designed the research. K.X., F.-H.W., and Z.-L.Z. performed the calculations. Z.-J.T., K.X., F.-H.W., G.X., and Z.-L.Z. analyzed the data. K.X., F.-H.W., and Z.J.T. wrote the manuscript. All authors discussed the results and reviewed the manuscript.

ACKNOWLEDGMENTS

We are grateful to Profs. Xiangyun Qiu (George Washington University), Shi-Jie Chen (University of Missouri), Wenbing Zhang (Wuhan University), Dr. Xi Zhang (Wuhan University) and Dr. Yuan-Yan Wu (Yangzhou University) for valuable discussions. We also thank Chang Shu for facility assistance. Parts of the numerical calculation in this work were performed on the supercomputing system in the Supercomputing Center of Wuhan University.

This work is supported by the National Science Foundation of China grants 11374234, 11575128, 11175132, and 11647312.

REFERENCES

1. Woodson, S. A. 2005. Metal ions and RNA folding: a highly charged topic with a dynamic future. *Curr. Opin. Chem. Biol.* 9:104–109.
2. Wong, G. C., and L. Pollack. 2010. Electrostatics of strongly charged biological polymers: ion-mediated interactions and self-organization in nucleic acids and proteins. *Annu. Rev. Phys. Chem.* 61:171–189.
3. Chen, S. J. 2008. RNA folding: conformational statistics, folding kinetics, and ion electrostatics. *Annu. Rev. Biophys.* 37:197–214.
4. Lipfert, J., S. Doniach, …, D. Herschlag. 2014. Understanding nucleic acid-ion interactions. *Annu. Rev. Biochem.* 83:813–841.
5. Jacobson, D. R., and O. A. Saleh. 2017. Counting the ions surrounding nucleic acids. *Nucleic Acids Res.* 45:1596–1605.
6. Bloomfield, V. A., D. M. Crothers, and I. Tinoco, Jr. 2000. Nucleic Acids: Structures, Properties, and Functions. University Science Books, Sausalito, CA.
7. Tan, Z. J., and S. J. Chen. 2011. Importance of diffuse metal ion binding to RNA. *Met. Ions Life Sci.* 9:101–124.
8. Bowman, J. C., T. K. Lenz, …, L. D. Williams. 2012. Cations in charge: magnesium ions in RNA folding and catalysis. *Curr. Opin. Struct. Biol.* 22:262–272.
9. Erat, M. C., J. Coles, …, R. K. Sigel. 2012. Accurate analysis of Mg^{2+} binding to RNA: from classical methods to a novel iterative calculation procedure. *Coord. Chem. Rev.* 256:279–288.
10. Auffinger, P., and E. Westhof. 1998. Simulations of the molecular dynamics of nucleic acids. *Curr. Opin. Struct. Biol.* 8:227–236.
11. Sun, L. Z., D. Zhang, and S. J. Chen. 2017. Theory and modeling of RNA structure and interactions with metal ions and small molecules. *Annu. Rev. Biophys.* 46:227–246.
12. Bukhman, Y. V., and D. E. Draper. 1997. Affinities and selectivities of divalent cation binding sites within an RNA tertiary structure. *J. Mol. Biol.* 273:1020–1031.
13. Denesyuk, N. A., and D. Thirumalai. 2015. How do metal ions direct ribozyme folding? *Nat. Chem.* 7:793–801.
14. Meisburger, S. P., S. A. Pabit, and L. Pollack. 2015. Determining the locations of ions and water around DNA from X-ray scattering measurements. *Biophys. J.* 108:2886–2895.

15. Record, M. T., Jr., M. L. Lohman, and P. De Haseth. 1976. Ion effects on ligand-nucleic acid interactions. *J. Mol. Biol.* 107:145–158.
16. Record, M. T., Jr., P. L. deHaseth, and T. M. Lohman. 1977. Interpretation of monovalent and divalent cation effects on the lac repressor-operator interaction. *Biochemistry.* 16:4791–4796.
17. Olmsted, M. C., C. F. Anderson, and M. T. Record, Jr. 1989. Monte Carlo description of oligoelectrolyte properties of DNA oligomers: range of the end effect and the approach of molecular and thermodynamic properties to the polyelectrolyte limits. *Proc. Natl. Acad. Sci. USA.* 86:7766–7770.
18. Olmsted, M. C., C. F. Anderson, and M. T. Record, Jr. 1991. Importance of oligoelectrolyte end effects for the thermodynamics of conformational transitions of nucleic acid oligomers: a grand canonical Monte Carlo analysis. *Biopolymers.* 31:1593–1604.
19. Olmsted, M. C., J. P. Bond, …, M. T. Record, Jr. 1995. Grand canonical Monte Carlo molecular and thermodynamic predictions of ion effects on binding of an oligocation (L^{8+}) to the center of DNA oligomers. *Biophys. J.* 68:634–647.
20. Ni, H., C. F. Anderson, and M. T. Record. 1999. Quantifying the thermodynamic consequences of cation (M^{2+}, M^{+}) accumulation and anion (X^{-}) exclusion in mixed salt solutions of polyanionic DNA using Monte Carlo and Poisson-Boltzmann calculations of ion-polyion preferential interaction coefficients. *J. Phys. Chem. B.* 103:3489–3504.
21. Shkel, I. A., and M. T. Record, Jr. 2004. Effect of the number of nucleic acid oligomer charges on the salt dependence of stability (DeltaG 37degrees) and melting temperature (Tm): NLPB analysis of experimental data. *Biochemistry.* 43:7090–7101.
22. Shkel, I. A., J. D. Ballin, and M. T. Record, Jr. 2006. Interactions of cationic ligands and proteins with small nucleic acids: analytic treatment of the large coulombic end effect on binding free energy as a function of salt concentration. *Biochemistry.* 45:8411–8426.
23. Shkel, I. A., and M. T. Record, Jr. 2012. Coulombic free energy and salt ion association per phosphate of all-atom models of DNA oligomer: dependence on oligomer size. *Soft Matter.* 8:9345–9355.
24. Korolev, N., N. V. Berezhnoy, …, L. Nordenskiöld. 2009. A universal description for the experimental behavior of salt-(in)dependent oligocation-induced DNA condensation. *Nucleic Acids Res.* 37:7137–7150.
25. Korolev, N., A. P. Lyubartsev, …, L. Nordenskiöld. 1999. Competitive binding of Mg^{2+}, Ca^{2+}, Na^{+}, and K^{+} ions to DNA in oriented DNA fibers: experimental and Monte Carlo simulation results. *Biophys. J.* 77:2736–2749.
26. Petrov, A. S., J. C. Bowman, …, L. D. Williams. 2011. Bidentate RNA-magnesium clamps: on the origin of the special role of magnesium in RNA folding. *RNA.* 17:291–297.
27. Kirmizialtin, S., and R. Elber. 2010. Computational exploration of mobile ion distributions around RNA duplex. *J. Phys. Chem. B.* 114:8207–8220.
28. Kirmizialtin, S., S. A. Pabit, …, R. Elber. 2012. RNA and its ionic cloud: solution scattering experiments and atomically detailed simulations. *Biophys. J.* 102:819–828.
29. Drozdetski, A. V., I. S. Tolokh, …, A. V. Onufriev. 2016. Opposing effects of multivalent ions on the flexibility of DNA and RNA. *Phys. Rev. Lett.* 117:028101.
30. Qiu, X., K. Andresen, …, L. Pollack. 2007. Inter-DNA attraction mediated by divalent counterions. *Phys. Rev. Lett.* 99:038104.
31. Qiu, X., K. Andresen, …, L. Pollack. 2008. Abrupt transition from a free, repulsive to a condensed, attractive DNA phase, induced by multivalent polyamine cations. *Phys. Rev. Lett.* 101:228101.
32. Qiu, X., V. A. Parsegian, and D. C. Rau. 2010. Divalent counterion-induced condensation of triple-strand DNA. *Proc. Natl. Acad. Sci. USA.* 107:21482–21486.
33. Qiu, X., D. C. Rau, …, W. M. Gelbart. 2011. Salt-dependent DNA-DNA spacings in intact bacteriophage λ reflect relative importance of DNA self-repulsion and bending energies. *Phys. Rev. Lett.* 106:028102.
34. Wu, Y. Y., Z. L. Zhang, …, Z. J. Tan. 2015. Multivalent ion-mediated nucleic acid helix-helix interactions: RNA versus DNA. *Nucleic Acids Res.* 43:6156–6165.
35. Cate, J. H., and J. A. Doudna. 1996. Metal-binding sites in the major groove of a large ribozyme domain. *Structure.* 4:1221–1229.
36. Shi, Y. Z., L. Jin, …, Z. J. Tan. 2015. Predicting 3D structure, flexibility, and stability of RNA hairpins in monovalent and divalent ion solutions. *Biophys. J.* 109:2654–2665.
37. Misra, V. K., and D. E. Draper. 2001. A thermodynamic framework for Mg^{2+} binding to RNA. *Proc. Natl. Acad. Sci. USA.* 98:12456–12461.
38. Draper, D. E. 2008. RNA folding: thermodynamic and molecular descriptions of the roles of ions. *Biophys. J.* 95:5489–5495.
39. Koculi, E., C. Hyeon, …, S. A. Woodson. 2007. Charge density of divalent metal cations determines RNA stability. *J. Am. Chem. Soc.* 129:2676–2682.
40. Schlick, T. 2002. Molecular Modeling and Simulation: An Interdisciplinary Guide. Springer, New York.
41. Kim, T., B. D. Freudenthal, …, T. Schlick. 2016. Insertion of oxidized nucleotide triggers rapid DNA polymerase opening. *Nucleic Acids Res.* 44:4409–4424.
42. Wang, J., Y. Zhao, …, Y. Xiao. 2015. Computational study of stability of an H-H-type pseudoknot motif. *Phys. Rev. E Stat. Nonlin. Soft Matter Phys.* 92:062705.
43. Wang, J., and Y. Xiao. 2016. Types and concentrations of metal ions affect local structure and dynamics of RNA. *Phys. Rev. E.* 94:040401.
44. Zhang, Y., J. Zhang, and W. Wang. 2011. Atomistic analysis of pseudoknotted RNA unfolding. *J. Am. Chem. Soc.* 133:6882–6885.
45. Bian, Y., C. Tan, …, W. Wang. 2014. Atomistic picture for the folding pathway of a hybrid-1 type human telomeric DNA G-quadruplex. *PLoS Comput. Biol.* 10:e1003562.
46. Manning, G. S. 1978. The molecular theory of polyelectrolyte solutions with applications to the electrostatic properties of polynucleotides. *Q. Rev. Biophys.* 11:179–246.
47. Manning, G. S. 2007. Counterion condensation on charged spheres, cylinders, and planes. *J. Phys. Chem. B.* 111:8554–8559.
48. Guéron, M., and G. Weisbuch. 1980. Polyelectrolyte theory. I. Counterion accumulation, site-binding, and their insensitivity to polyelectrolyte shape in solutions containing finite salt concentrations. *Biopolymers.* 19:353–382.
49. Baker, N. A., D. Sept, …, J. A. McCammon. 2001. Electrostatics of nanosystems: application to microtubules and the ribosome. *Proc. Natl. Acad. Sci. USA.* 98:10037–10041.
50. Baker, N. A. 2005. Improving implicit solvent simulations: a Poisson-centric view. *Curr. Opin. Struct. Biol.* 15:137–143.
51. Sushko, M. L., D. G. Thomas, …, N. A. Baker. 2016. The role of correlation and solvation in ion interactions with B-DNA. *Biophys. J.* 110:315–326.
52. Tan, Z. J., and S. J. Chen. 2005. Electrostatic correlations and fluctuations for ion binding to a finite length polyelectrolyte. *J. Chem. Phys.* 122:44903.
53. Tan, Z. J., and S. J. Chen. 2006. Electrostatic free energy landscapes for nucleic acid helix assembly. *Nucleic Acids Res.* 34:6629–6639.
54. Tan, Z. J., and S. J. Chen. 2010. Predicting ion binding properties for RNA tertiary structures. *Biophys. J.* 99:1565–1576.
55. Giambaşu, G. M., T. Luchko, …, D. A. Case. 2014. Ion counting from explicit-solvent simulations and 3D-RISM. *Biophys. J.* 106:883–894.
56. Lu, B. Z., Y. C. Zhou, …, J. A. McCammon. 2008. Recent progress in numerical methods for the Poisson-Boltzmann equation in biophysical applications. *Commun. Comput. Phys.* 3:973–1009.
57. Chen, D., Z. Chen, …, G. W. Wei. 2011. MIBPB: a software package for electrostatic analysis. *J. Comput. Chem.* 32:756–770.
58. Wei, G. W., Q. Zheng, …, K. Xia. 2012. Variational multiscale models for charge transport. *SIAM Rev. Soc. Ind. Appl. Math.* 54:699–754.

59. Liu, H. Y., and X. Zou. 2006. Electrostatics of ligand binding: parametrization of the generalized Born model and comparison with the Poisson-Boltzmann approach. *J. Phys. Chem. B.* 110:9304–9313.

60. Zhang, X., J. S. Zhang, …, Z. J. Tan. 2016. Potential of mean force between like-charged nanoparticles: many-body effect. *Sci. Rep.* 6:23434.

61. Tan, Z. J., and S. J. Chen. 2006. Nucleic acid helix stability: effects of salt concentration, cation valence and size, and chain length. *Biophys. J.* 90:1175–1190.

62. Tan, Z. J., and S. J. Chen. 2011. Salt contribution to RNA tertiary structure folding stability. *Biophys. J.* 101:176–187.

63. Bai, Y., M. Greenfeld, …, D. Herschlag. 2007. Quantitative and comprehensive decomposition of the ion atmosphere around nucleic acids. *J. Am. Chem. Soc.* 129:14981–14988.

64. Tan, Z. J., and S. J. Chen. 2012. Ion-mediated RNA structural collapse: effect of spatial confinement. *Biophys. J.* 103:827–836.

65. Bao, L., X. Zhang, …, Z. J. Tan. 2017. Understanding the relative flexibility of RNA and DNA duplexes: stretching and twist-stretch coupling. *Biophys. J.* 112:1094–1104.

66. Kirmizialtin, S., A. R. Silalahi, …, M. O. Fenley. 2012. The ionic atmosphere around A-RNA: Poisson-Boltzmann and molecular dynamics simulations. *Biophys. J.* 102:829–838.

67. Simonov, N. A., M. Mascagni, and M. O. Fenley. 2007. Monte Carlo-based linear Poisson-Boltzmann approach makes accurate salt-dependent solvation free energy predictions possible. *J. Chem. Phys.* 127:185105.

68. Hayes, R. L., J. K. Noel, …, J. N. Onuchic. 2014. Reduced model captures $Mg^{(2+)}$-RNA interaction free energy of riboswitches. *Biophys. J.* 106:1508–1519.

69. Shi, Y. Z., F. H. Wang, …, Z. J. Tan. 2014. A coarse-grained model with implicit salt for RNAs: predicting 3D structure, stability and salt effect. *J. Chem. Phys.* 141:105102.

70. Auffinger, P., L. Bielecki, and E. Westhof. 2003. The Mg^{2+} binding sites of the 5S rRNA loop E motif as investigated by molecular dynamics simulations. *Chem. Biol.* 10:551–561.

71. Auffinger, P., L. Bielecki, and E. Westhof. 2004. Symmetric K+ and Mg2+ ion-binding sites in the 5S rRNA loop E inferred from molecular dynamics simulations. *J. Mol. Biol.* 335:555–571.

72. Robbins, T. J., J. D. Ziebarth, and Y. Wang. 2014. Comparison of monovalent and divalent ion distributions around a DNA duplex with molecular dynamics simulation and a Poisson-Boltzmann approach. *Biopolymers.* 101:834–848.

73. Hayes, R. L., J. K. Noel, …, K. Y. Sanbonmatsu. 2012. Magnesium fluctuations modulate RNA dynamics in the SAM-I riboswitch. *J. Am. Chem. Soc.* 134:12043–12053.

74. Li, W., L. Nordenskiöld, and Y. Mu. 2011. Sequence-specific Mg^{2+}-DNA interactions: a molecular dynamics simulation study. *J. Phys. Chem. B.* 115:14713–14720.

75. Pan, F., C. Roland, and C. Sagui. 2014. Ion distributions around left- and right-handed DNA and RNA duplexes: a comparative study. *Nucleic Acids Res.* 42:13981–13996.

76. Qi, W., X. Lei, and H. Fang. 2010. DNA structural changes under different stretching methods studied by molecular dynamics simulations. *ChemPhysChem.* 11:2146–2151.

77. Qi, W., B. Song, …, H. Fang. 2011. DNA base pair hybridization and water-mediated metastable structures studied by molecular dynamics simulations. *Biochemistry.* 50:9628–9632.

78. Zhang, X., L. Bao, …, Z. J. Tan. 2017. Radial distribution function of semiflexible oligomers with stretching flexibility. *J. Chem. Phys.* 147:054901.

79. Wu, Y. Y., L. Bao, …, Z. J. Tan. 2015. Flexibility of short DNA helices with finite-length effect: from base pairs to tens of base pairs. *J. Chem. Phys.* 142:125103.

80. Zhang, Z. L., Y. Y. Wu, …, Z. J. Tan. 2017. Divalent ion-mediated DNA-DNA interactions: a comparative study of triplex and duplex. *Biophys. J.* 113:517–528.

81. Yoo, J., and A. Aksimentiev. 2012. Improved parametrization of Li^+, Na^+, K^+, and Mg^{2+} ions for all-atom molecular dynamics simulations of nucleic acid systems. *J. Phys. Chem. Lett.* 3:45–50.

82. Yoo, J., and A. Aksimentiev. 2012. Competitive binding of cations to duplex DNA revealed through molecular dynamics simulations. *J. Phys. Chem. B.* 116:12946–12954.

83. Xu, X., T. Yu, and S. J. Chen. 2016. Understanding the kinetic mechanism of RNA single base pair formation. *Proc. Natl. Acad. Sci. USA.* 113:116–121.

84. Wang, Y., S. Gong, …, W. Zhang. 2016. The thermodynamics and kinetics of a nucleotide base pair. *J. Chem. Phys.* 144:115101.

85. Savelyev, A., and A. D. MacKerell, Jr. 2015. Competition among $Li^{(+)}$, $Na^{(+)}$, $K^{(+)}$, and $Rb^{(+)}$ monovalent ions for DNA in molecular dynamics simulations using the additive CHARMM36 and Drude polarizable force fields. *J. Phys. Chem. B.* 119:4428–4440.

86. Bergonzo, C., K. B. Hall, and T. E. Cheatham, III. 2016. Divalent ion dependent conformational changes in an RNA stem-loop observed by molecular dynamics. *J. Chem. Theory Comput.* 12:3382–3389.

87. Bergonzo, C., and T. E. Cheatham, III. 2017. Mg^{2+} binding promotes SLV as a scaffold in varkud satellite ribozyme SLI-SLV kissing loop junction. *Biophys. J.* 113:313–320.

88. Su, L., L. Chen, …, A. Rich. 1999. Minor groove RNA triplex in the crystal structure of a ribosomal frameshifting viral pseudoknot. *Nat. Struct. Biol.* 6:285–292.

89. Conn, G. L., A. G. Gittis, …, D. E. Draper. 2002. A compact RNA tertiary structure contains a buried backbone-K+ complex. *J. Mol. Biol.* 318:963–973.

90. Westhof, E., and M. Sundaralingam. 1986. Restrained refinement of the monoclinic form of yeast phenylalanine transfer RNA. Temperature factors and dynamics, coordinated waters, and base-pair propeller twist angles. *Biochemistry.* 25:4868–4878.

91. Montange, R. K., and R. T. Batey. 2006. Structure of the S-adenosylmethionine riboswitch regulatory mRNA element. *Nature.* 441:1172–1175.

92. Pérez, A., I. Marchán, …, M. Orozco. 2007. Refinement of the AMBER force field for nucleic acids: improving the description of α/λ conformers. *Biophys. J.* 92:3817–3829.

93. Rose, P. W., A. Prlić, …, S. K. Burley. 2017. The RCSB protein data bank: integrative view of protein, gene and 3D structural information. *Nucleic Acids Res.* 45:D271–D281.

94. Joung, I. S., and T. E. Cheatham, III. 2008. Determination of alkali and halide monovalent ion parameters for use in explicitly solvated biomolecular simulations. *J. Phys. Chem. B.* 112:9020–9041.

95. Åqvist, J. 1990. Ion-water interaction potentials derived from free energy pertubation simulations. *J. Phys. Chem.* 94:8021–8024.

96. Hess, B., C. Kutzner, …, E. Lindahl. 2008. GROMACS 4: algorithms for highly efficient, load-balanced, and scalable molecular simulation. *J. Chem. Theory Comput.* 4:435–447.

97. Essmann, U., L. Perera, …, L. G. Pedersen. 1995. A smooth particle mesh Ewald method. *J. Chem. Phys.* 103:8577–8593.

98. Allnér, O., L. Nilsson, and A. Villa. 2012. Magnesium ion-water coordination and exchange in biomolecular simulations. *J. Chem. Theory Comput.* 8:1493–1502.

99. Li, P., B. P. Roberts, …, K. M. Merz, Jr. 2013. Rational design of particle mesh Ewald compatible Lennard-Jones parameters for +2 metal cations in explicit solvent. *J. Chem. Theory Comput.* 9:2733–2748.

100. Humphrey, W., A. Dalke, and K. Schulten. 1996. VMD: visual molecular dynamics. *J. Mol. Graph.* 14:33–38.

101. Marcus, Y. 1985. Ion Solvation. Wiley, Hoboken, NJ.

102. Simonin, J. P., L. Blum, and P. Turq. 1996. Real ionic solutions in the mean spherical approximation. 1. Simple salts in the primitive model. *J. Phys. Chem.* 100:7704–7709.

103. Lavery, R., M. Moakher, …, K. Zakrzewska. 2009. Conformational analysis of nucleic acids revisited: Curves+. *Nucleic Acids Res.* 37:5917–5929.

Biophysical Journal, Volume *114*

Supplemental Information

Competitive Binding of Mg^{2+} and Na^{+} Ions to Nucleic Acids: From Helices to Tertiary Structures

Kun Xi, Feng-Hua Wang, Gui Xiong, Zhong-Liang Zhang, and Zhi-Jie Tan

The ellipsoid representation for a nucleic acid

Since the surface charge density cannot be well defined for a nucleic acid with complex structure, we would approximately model a nucleic acid as an ellipsoid so as to estimate the surface charge density σ_{eff} for the nucleic acid, with its center of mass located at the original point. The three radii r_α (α=1, 2, 3) of the ellipsoid for a nucleic acid are determined by solving (1,2)

$$\boldsymbol{I}\boldsymbol{\omega}_\alpha=\lambda_\alpha\boldsymbol{\omega}_\alpha;\ I_{ij}=\sum_{k=1}^{N-1}(\mathbf{r}_k^2\delta_{ij}-\mathrm{r}_{k,i}\mathrm{r}_{k,j});\ r_\alpha^2=\sum_{\alpha^*=1}^{3}(-1)^{\delta_{\alpha\alpha^*}}\lambda_{\alpha^*}, \quad (1)$$

where $\boldsymbol{I}$ represents the matrix of rotational inertia tensor I_{ij} (i, j=x, y, z), λ_α is the eigenvalue and $\boldsymbol{\omega}_\alpha$ is the eigenvector associated the radius r_α of the ellipsoid. The rotation inertia tensor I_{ij} (i, j=x, y, z) of a nucleic acid was calculated with only considering the phosphate atoms and $\mathbf{r}_k^2$=x_k^2+y_k^2+z_k^2, where the coordinates of the k-th phosphate atom are denoted by (x_k, y_k, z_k), and $\mathrm{r}_{k,i}$ means the i-coordinate of the k-th phosphate. Thus the surface area of the ellipsoid is $S=2\pi\sqrt{r_1^2r_2^2+r_1^2r_3^2+r_2^2r_3^2+r_1r_2r_3(r_1+r_2+r_3)/3}$ (1,2), and surface charge density σ_{eff} for the ellipsoid representation of a nucleic acid is approximated as $\sigma_{eff}=N/S$. The ellipsoid representations for the used nucleic acids are shown in Fig. S12.

Table S1 The sequences of dsDNA and dsRNAs used in the work[a].

Nucleic Acids	Sequences
24-bp dsDNA	5'-GGTGACGAGTGAGCTACTGGGCGG-3' CCACTGCTCACTCGATGACCCGCC
24-bp dsRNA	5'-GGUGACGAGUGAGCUACUGGGCGG-3' CCACUGCUCACUCGAUGACCCGCC
12-bp dsRNA	5'-GAGUGAGCUACU-3' CUCACUCGAUGA
8-bp dsRNA	5'-GUGAGCUA-3' CACUCGAU

[a]The sequences were selected according to the experiments by Bai et al (3) and the recent molecular dynamic simulations (4).

Table S2 The numbers of added ions and global binding ions[a].

DNA or RNAs	Desired bulk $[Mg^{2+}]/[Na^{+}]$ (mM)	N_{Mg}^{c}	N_{Na}^{c}	N_{Mg}	N_{Na}	N_{Cl}	$N_{Mg}^{b\ b}$	$N_{Na}^{b\ b}$	$N_{Cl}^{b\ b}$
24-bp dsDNA	1/20	14	18	15	42	26	12.48	15.84	-3.36
	5/20	19	8	25	32	36	18.24	3.84	-2.88
	5/40	16	14	22	62	60	16.32	9.12	-3.36
	5/70	14	18	20	103	97	12.48	16.10	-5.52
	5/240	7	32	13	324	304	6.44	24.38	-9.20
	5/420	4	38	10	550	524	3.68	27.60	-11.96
	10/20	20	6	32	30	48	18.86	3.68	-1.84
	20/20	21	4	45	28	72	19.32	1.38	-3.22
	50/20	22	2	82	26	144	19.78	0.92	-5.06
8-bp dsRNA	1/20	3	8	4	21	15	3.08	5.46	-2.30
	10/20	6	2	12	15	39	5.60	1.54	-1.21
12-bp dsRNA	1/20	5	12	6	27	17	5.28	8.14	-3.13
	10/20	9	4	16	19	29	9.02	1.98	-1.89
24-bp dsRNA	1/20	15	16	16	40	66	13.80	12.42	-5.68
	5/20	19	8	25	32	36	18.40	4.14	-4.73
	10/20	21	4	33	28	48	19.32	3.68	-3.47
	50/20	22	2	82	26	144	20.24	1.38	-4.07
28-nt BWYV pseudoknot	1/20	8	11	9	28	19	7.83	7.83	-3.21
	10/20	11	5	19	22	33	11.34	2.16	-2.03
58-nt rRNA fragment	1/20	20	17	21	41	26	18.81	11.40	-7.83
	10/20	25	7	37	31	48	25.08	2.28	-4.41
76-nt Yeast $tRNA^{Phe}$	1/20	27	21	28	57	38	24.01	18.02	-8.84
	10/20	34	7	52	43	72	32.25	4.50	-5.82
94-nt SAM-I riboswitch	1/20	34	25	35	54	31	30.69	16.74	-13.77
	10/20	43	7	57	36	57	42.78	3.72	-3.54

[a]The simulational cells for the respective cases are listed in Table I in the main text.

[b]The numbers of binding ions in excess of bulk ion concentration, which were defined as global binding ions, are calculated through Eq. 5 in the main text.

Table S3 The average number fractions of local binding ions within ~5 Å around phosphates[a].

RNAs and Desired bulk $[Mg^{2+}]/[Na^{+}]$ (mM)		N_P[b] 2	3	4	5	6
BWYV pseudoknot (1/20)	$\bar{f}_{Mg}$	0.043 ± 0.001	0.111 ± 0.024	0.186 ± 0.028	0.290 ± 0.053	0.315 ± 0.022
	$\bar{f}_{Na}$	0.016 ± 0.001	0.018 ± 0.002	0.030 ± 0.004	0.049 ± 0.006	0.048 ± 0.007
BWYV pseudoknot (10/20)	$\bar{f}_{Mg}$	0.063 ± 0.002	0.119 ± 0.022	0.313 ± 0.052	0.399 ± 0.055	0.422 ± 0.013
	$\bar{f}_{Na}$	0.003 ± 0.001	0.006 ± 0.001	0.010 ± 0.002	0.010 ± 0.002	0.009 ± 0.002
rRNA fragment (1/20)	$\bar{f}_{Mg}$	0.037 ± 0.001	0.111 ± 0.021	0.205 ± 0.015	0.304 ± 0.033	0.319 ± 0.022
	$\bar{f}_{Na}$	0.015 ± 0.001	0.021 ± 0.005	0.035 ± 0.002	0.045 ± 0.004	0.052 ± 0.006
rRNA fragment (10/20)	$\bar{f}_{Mg}$	0.059 ± 0.001	0.134 ± 0.035	0.304 ± 0.045	0.419 ± 0.015	0.433 ± 0.022
	$\bar{f}_{Na}$	0.003 ± 0.001	0.004 ± 0.001	0.010 ± 0.002	0.009 ± 0.001	0.009 ± 0.001
Yeast $tRNA^{Phe}$ (1/20)	$\bar{f}_{Mg}$	0.048 ± 0.001	0.103 ± 0.002	0.229 ± 0.043	0.311 ± 0.032	0.310 ± 0.012
	$\bar{f}_{Na}$	0.012 ± 0.002	0.022 ± 0.002	0.027 ± 0.003	0.049 ± 0.004	0.056 ± 0.003
Yeast $tRNA^{Phe}$ (10/20)	$\bar{f}_{Mg}$	0.067 ± 0.002	0.140 ± 0.021	0.293 ± 0.023	0.411 ± 0.042	0.422 ± 0.021
	$\bar{f}_{Na}$	0.004 ± 0.001	0.004 ± 0.001	0.009 ± 0.002	0.007 ± 0.001	0.010 ± 0.001
SAM-I riboswitch (1/20)	$\bar{f}_{Mg}$	0.050 ± 0.001	0.122 ± 0.022	0.202 ± 0.061	0.305 ± 0.035	0.313 ± 0.021
	$\bar{f}_{Na}$	0.022 ± 0.001	0.019 ± 0.001	0.030 ± 0.003	0.040 ± 0.001	0.062 ± 0.001
SAM-I riboswitch (10/20)	$\bar{f}_{Mg}$	0.070 ± 0.001	0.117 ± 0.026	0.296 ± 0.035	0.430 ± 0.055	0.441 ± 0.039
	$\bar{f}_{Na}$	0.001 ± 0.001	0.004 ± 0.001	0.013 ± 0.001	0.011 ± 0.002	0.010 ± 0.002

[a]The average number fractions of local binding Mg^{2+}/Na^{+} around phosphates within ~5 Å for RNA tertiary structures shown in Fig. 8B and C in the main text.

[b]The local phosphate density, i.e. the local number of phosphates closely around phosphates within ~9 Å, are calculated according to the phosphate-phosphate radial distribution function in Fig. S13A.

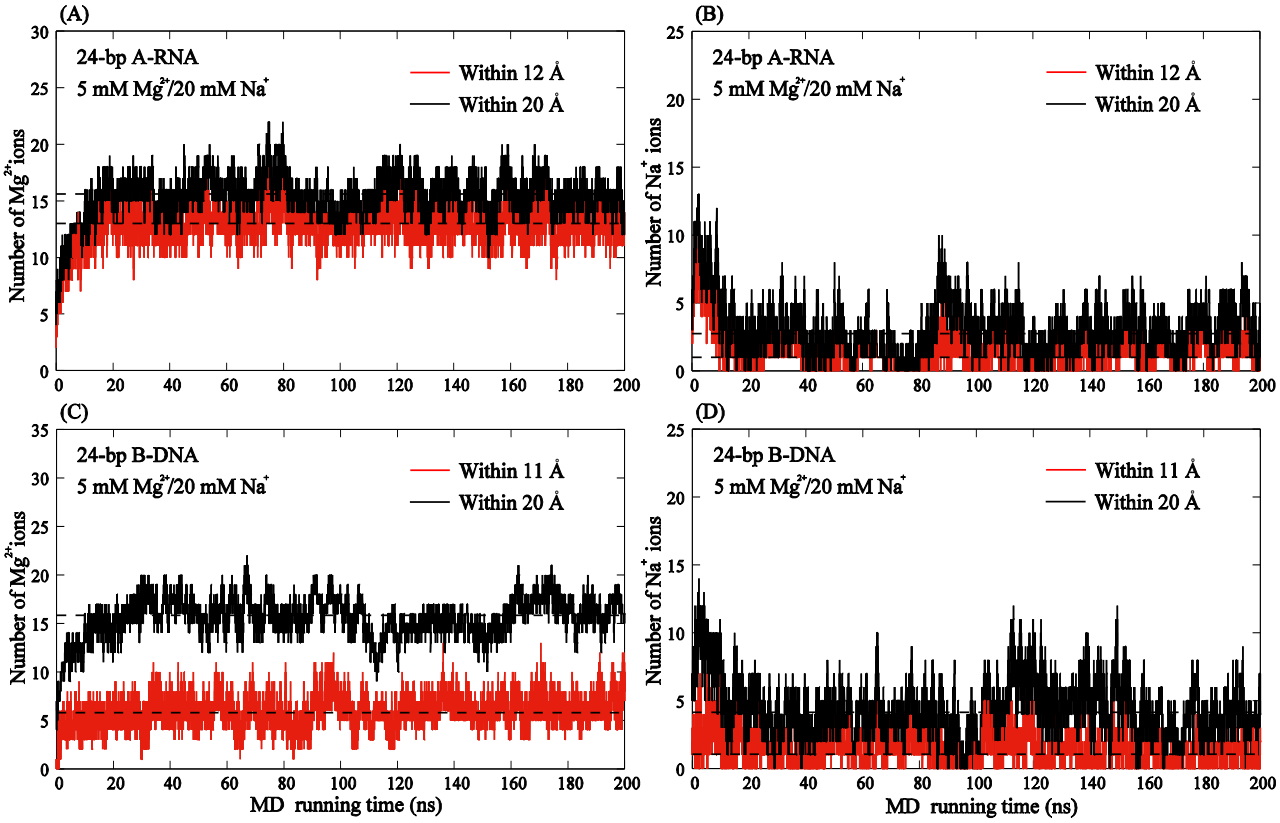

Figure S1 The numbers of Mg^{2+} (A,C) and Na^{+} (B,D) ions within the denoted distances from the central axis of the 24-bp dsRNA (A,B) and dsDNA (C,D) as functions of MD simulation time (ns). The dashed lines denote the averaged values in equilibrium. The two denoted distances approximately correspond to the helical radius and two times of helical radius for dsRNA and dsDNA, respectively.

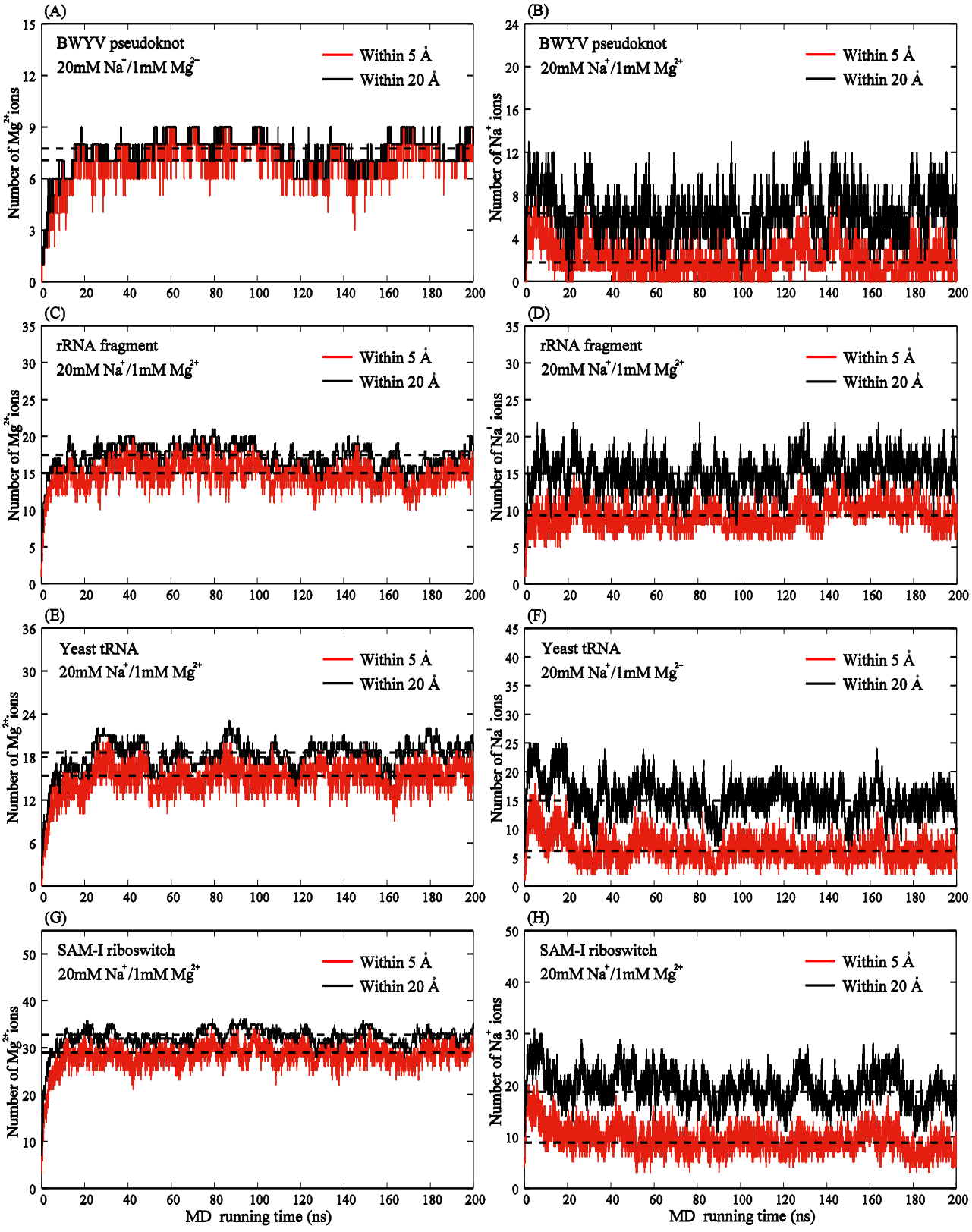

Figure S2 The numbers of Mg^{2+} (A,C,E,G) and Na^{+} (B,D,F,H) ions within the denoted distances from the surface atoms of BWYV pseudoknot (A,B), 58-nt rRNA fragment (C,D), yeast $tRNA^{Phe}$ (E,F) and SAM-I riboswitch (G,H) as functions of MD simulation time (ns). The dashed lines denote the averaged values in equilibrium. The two denoted distances approximately cover the first layer of Mg^{2+} and all the global binding ions, respectively; see Fig. S6 in the Supporting Materials.

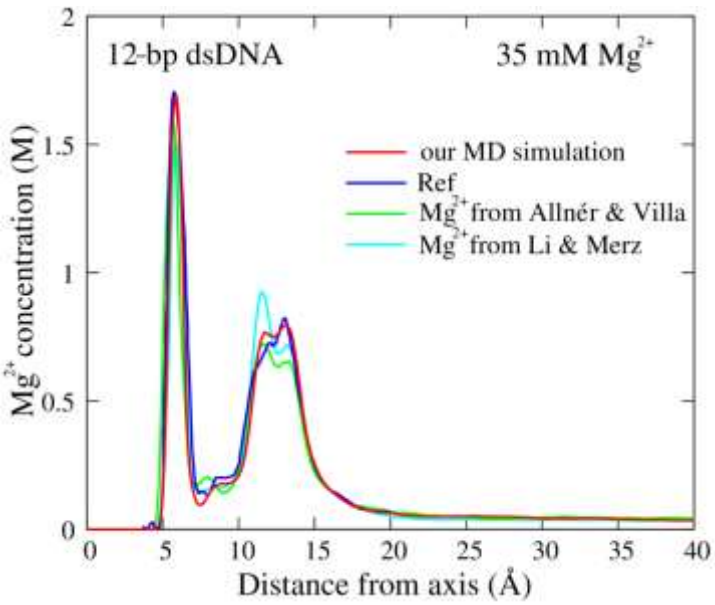

Figure S3 The radial concentration distributions of Mg^{2+} around the central axis of a 12-bp dsDNA. The red, blue, green and cyan lines denote the results from our simulations with Mg^{2+} force-field parameters from Ref (5), from Ref (6) and from Ref (7), respectively. In addition, the blue line is from the MD simulations of Robbins et al (8) with Mg^{2+} force-field parameter from Ref (5). The sequence of the 12-bp dsDNA is d(CGCGAATTCGCG) (8).

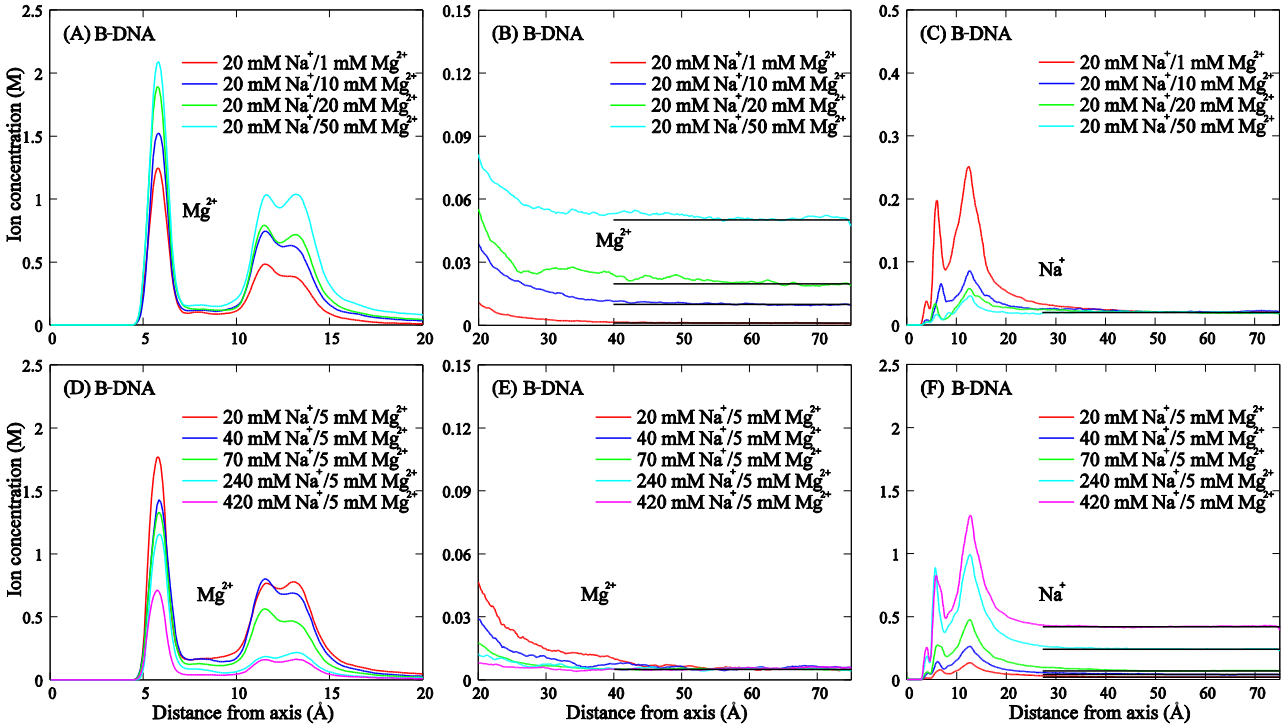

Figure S4 The radial concentration distributions of Mg^{2+} (A,B,D,E) and Na^{+} (C,F) around 24-bp dsDNA in mixed Mg^{2+}/Na^{+} solutions. (A-C) The solutions are with 20 mM Na^{+} and different [Mg^{2+}]'s; (D-F) The solutions are with 5 mM Mg^{2+} and different [Na^{+}]'s. The solid black lines denote the desired bulk Mg^{2+}/Na^{+} concentrations in our simulations.

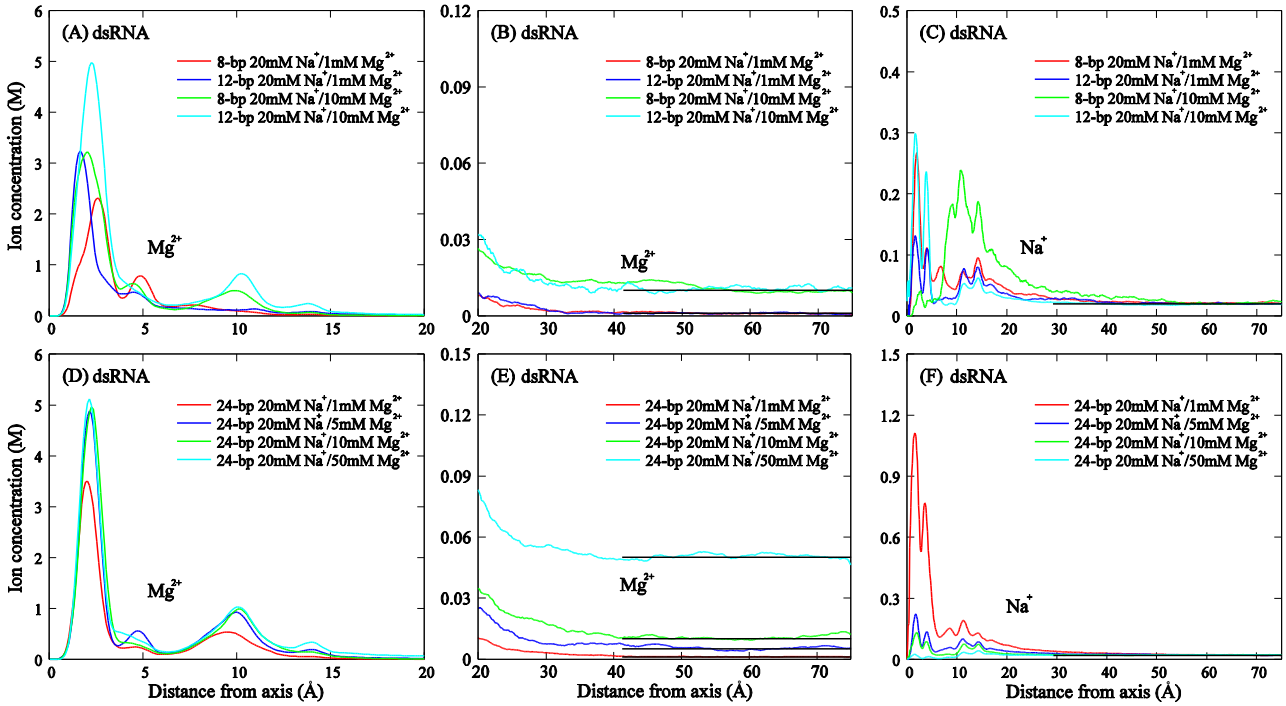

Figure S5 The radial concentration distributions of Mg^{2+} (A,B,D,E) and Na^{+} (C,F) around 8-bp, 12-bp and 24-bp dsRNAs in mixed Mg^{2+}/Na^{+} solutions. The solutions are with 20 mM Na^{+} and different [Mg^{2+}]'s, and the solid black lines denote the desired bulk Mg^{2+}/Na^{+} concentrations in our simulations.

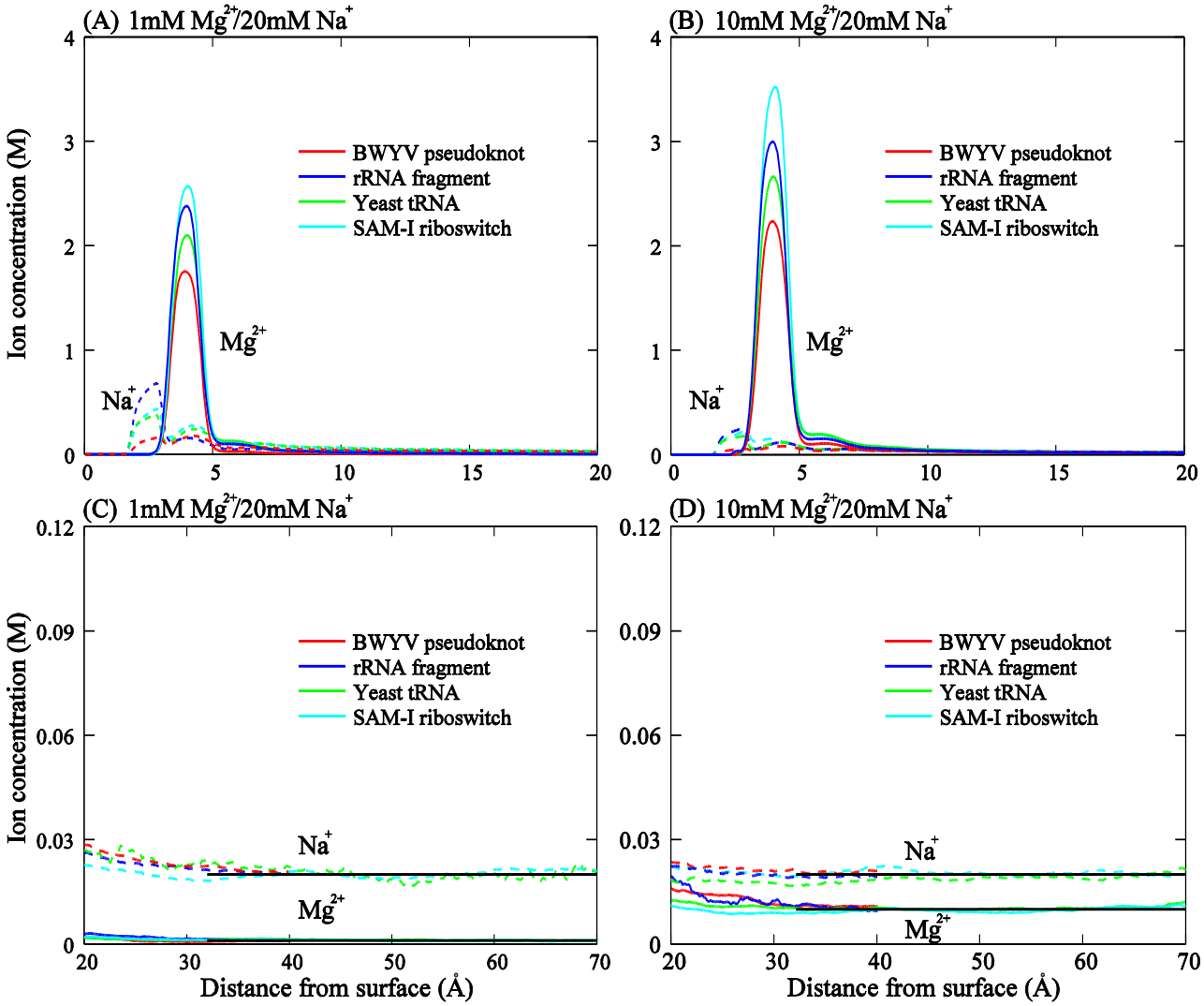

Figure S6 The concentration distributions of Mg^{2+} and Na^{+} around various RNA tertiary structures in mixed 1 mM Mg^{2+}/20 mM Na^{+} (A,C) and 10 mM Mg^{2+}/20 mM Na^{+} Mg^{2+}/Na^{+} (B,D) solutions. The RNA tertiary structures include BWYV pseudoknot (red), 58-nt rRNA fragment (blue), yeast $tRNA^{Phe}$ (green) and SAM-I riboswitch (cyan). The solid black lines denote the desired bulk Mg^{2+}/Na^{+} concentrations in our simulations.

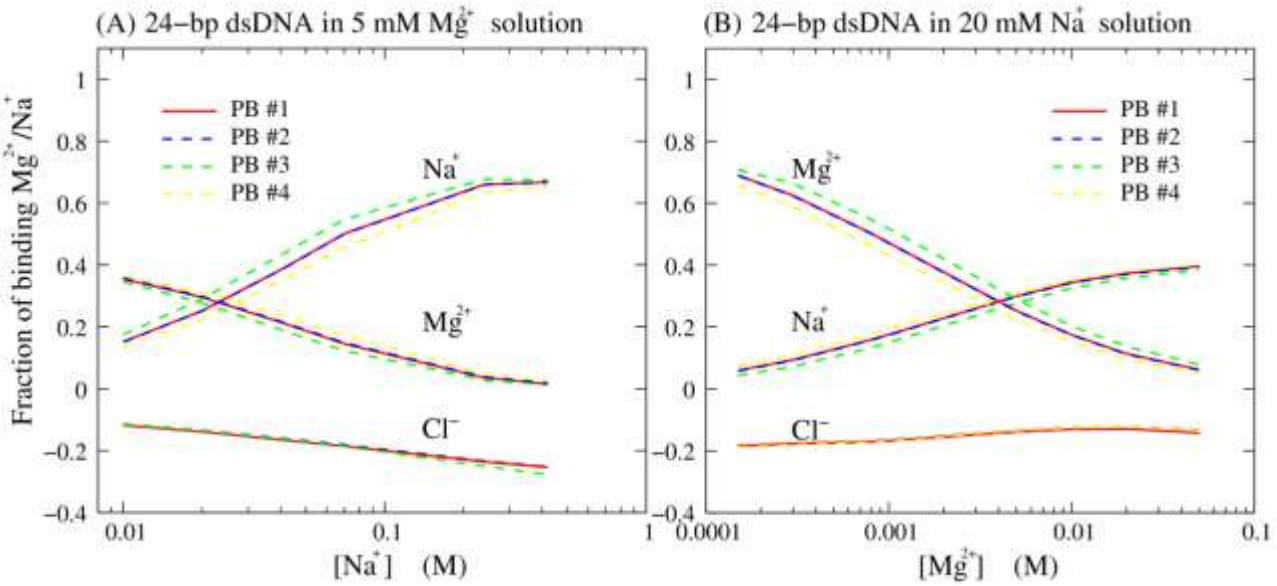

Figure S7 (A,B) The number fractions of binding Mg^{2+}, Na^{+} and Cl^{-} per nucleotide for the 24-bp dsDNA from the PB calculations as functions of [Na^{+}] (A) and [Mg^{2+}] (B). PB #1: the dielectric constant of DNA is 2 and the radii of Mg^{2+}/Na^{+} are 3.0 and 2.0 Å; PB #2: the dielectric constant of DNA is 10 and the radii of Mg^{2+}/Na^{+} are 3.0 and 2.0 Å; PB #3: the dielectric constant of DNA is 2 and the radii of Mg^{2+}/Na^{+} are 3.6 and 2.0 Å; PB #4: the dielectric constant of DNA is 2 and the radii of Mg^{2+}/Na^{+} are 3.0 and 2.7 Å.

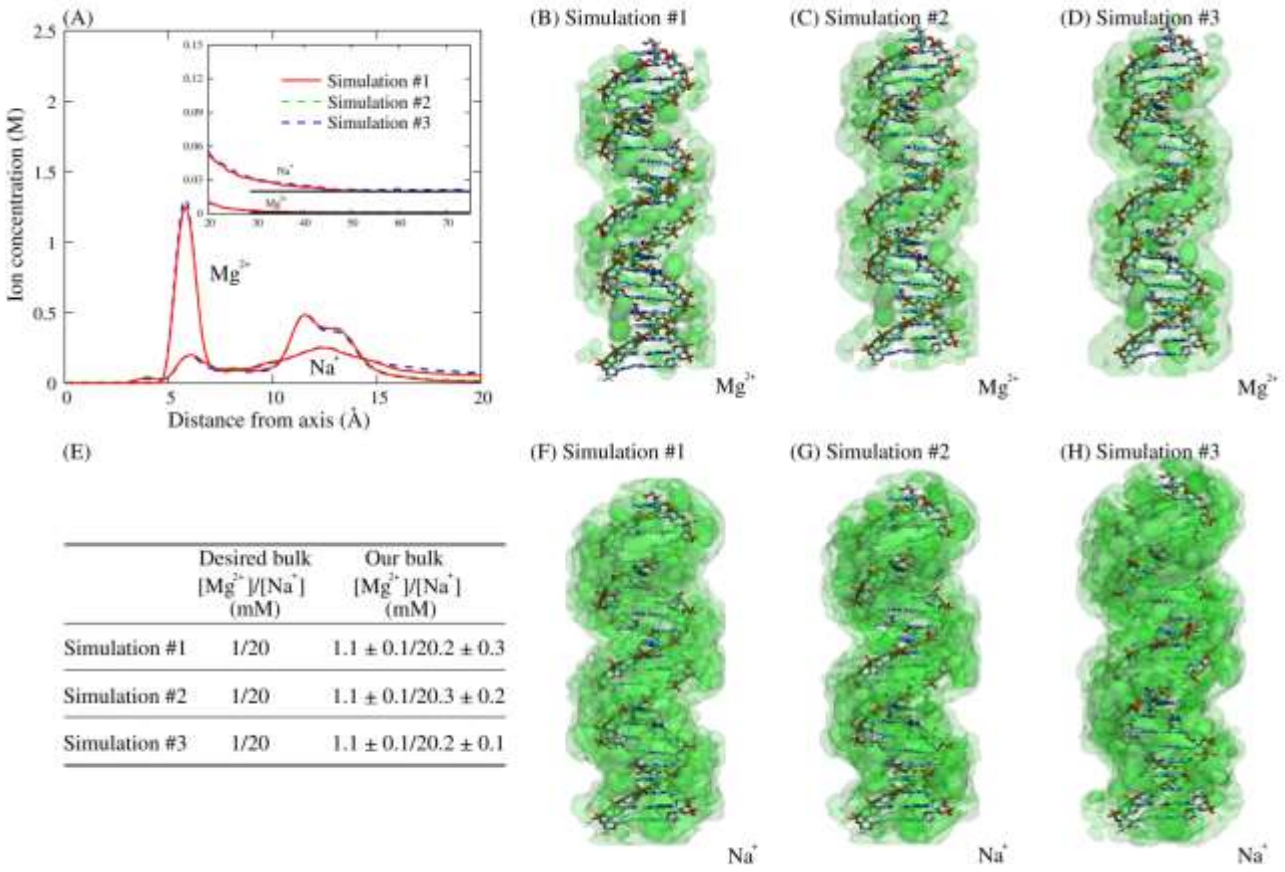

	Desired bulk $[Mg^{2+}]/[Na^{+}]$ (mM)	Our bulk $[Mg^{2+}]/[Na^{+}]$ (mM)
Simulation #1	1/20	1.1 ± 0.1/20.2 ± 0.3
Simulation #2	1/20	1.1 ± 0.1/20.3 ± 0.2
Simulation #3	1/20	1.1 ± 0.1/20.2 ± 0.1

Figure S8 (A) The radial concentration distribution of Mg^{2+} and Na^{+} around 24-bp dsDNA in 1 mM Mg^{2+}/20 mM Na^{+} solution from the original simulation (simulation #1) and two additional simulations (the simulation with different initial ions positions, named as simulations #2; and the simulation with longer size (~120 Å) in the z-axis, named as simulation #3). (B,C,D,F,G,H) The spatial ion concentration of Mg^{2+} and Na^{+} around 24-bp dsDNA for the three simulations were displayed in green of three-level opacities (0.5 M-5 M, 5 M-10 M and >10 M for Mg^{2+} and 0.25 M-0.5 M, 0.5 M-2.0 M, >2.0 M for Na^{+}) by VMD (10). (E) The bulk ion concentrations of Mg^{2+}/Na^{+} obtained from the three simulations, respectively.

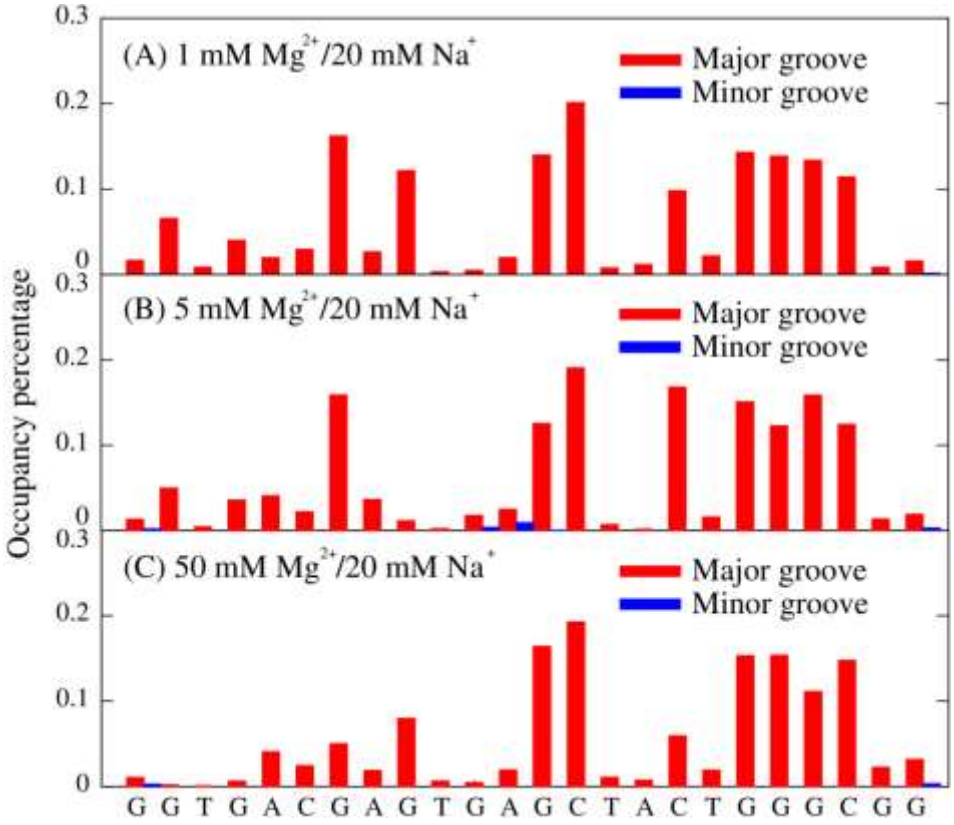

Figure S9 The number fractions of binding ions in the major groove and the minor groove per base pair of 24-bp dsDNA, which were calculated as those within a distance of 4.5 Å from the atoms labeled in previous simulation work (9).

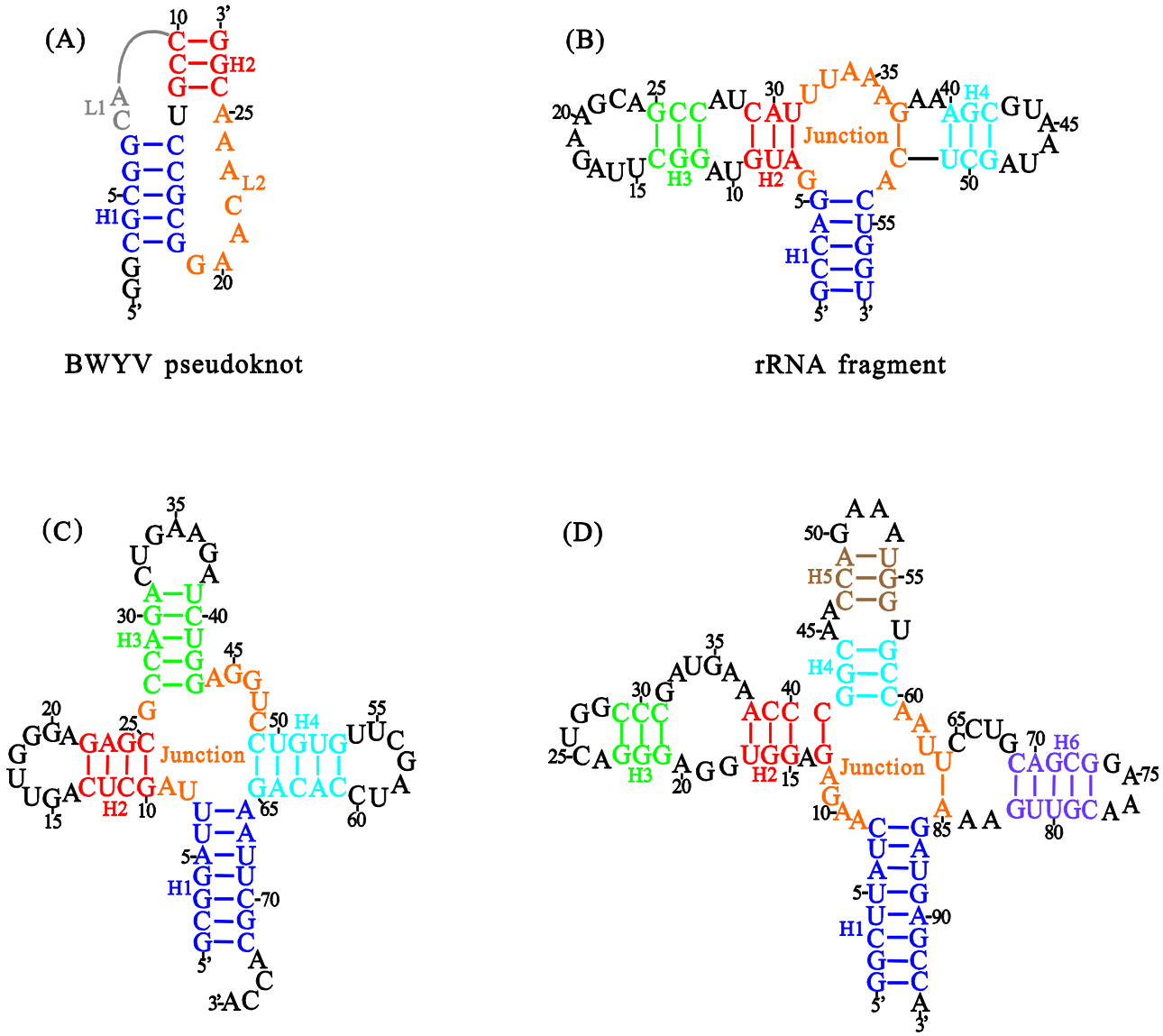

Figure S10 The secondary structures for 28-nt BWYV pseudoknot (A), 58-nt rRNA fragment (B), 76-nt yeast $tRNA^{Phe}$ (C) and 94-nt SAM-I riboswitch (D). Here, the names of helical stems, loops and junction are corresponding to those of respective 3D structures in Fig. 7 in the main text and Fig. S11 in the Supporting Materials.

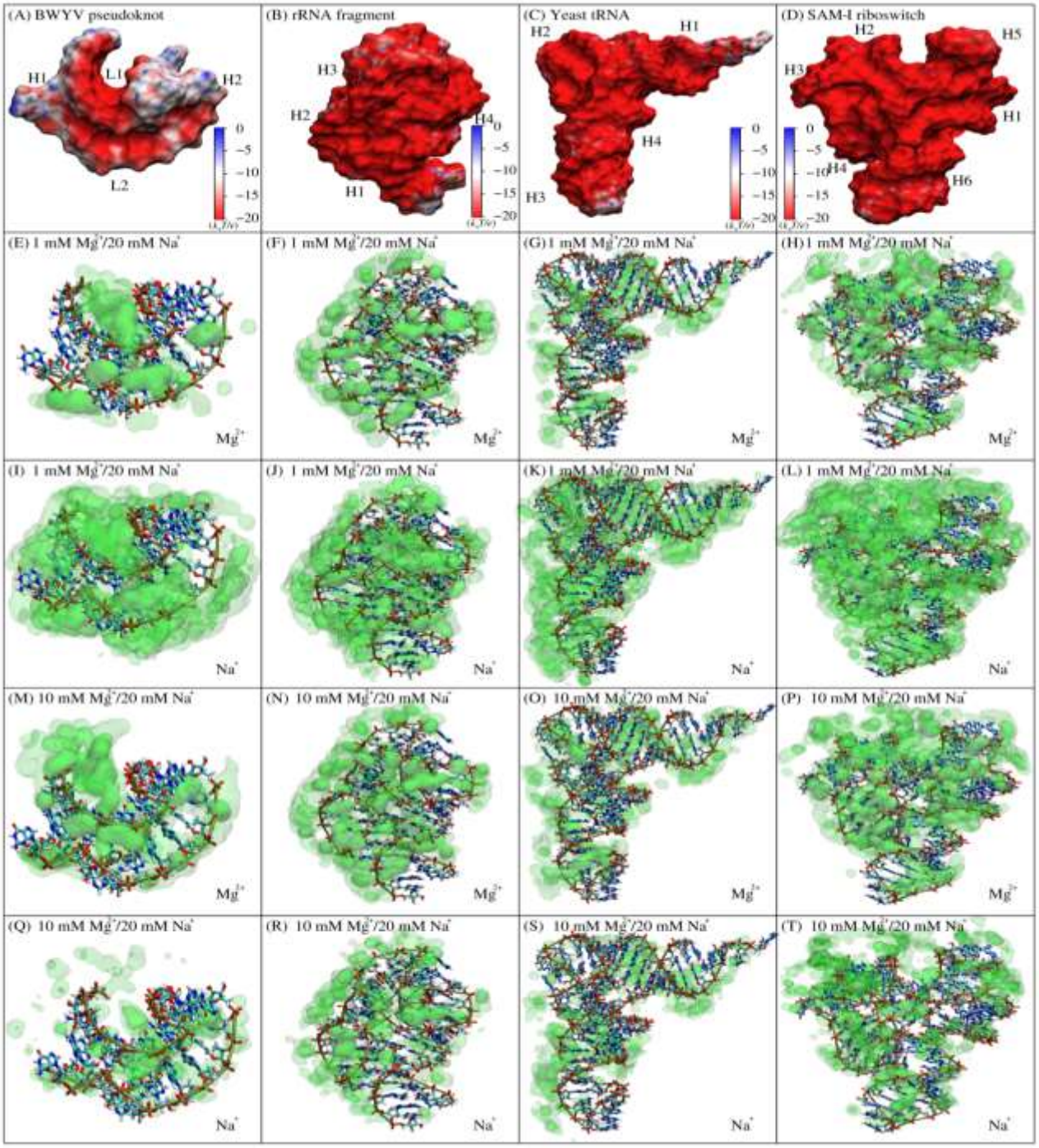

Figure S11 (A-D) The electrostatic potentials at the Mg^{2+} accessible surface of BWYV pseudoknot (A), 58-nt rRNA fragment (B), yeast $tRNA^{Phe}$ (C) and SAM-I riboswitch (D) were calculated by APBS (10). Shown is the electrostatic potential computed 3 Å away (radius of hydrated Mg^{2+} is ~3 Å (12)) from the surface by VMD (11). (E-T) The spatial ion concentration of Mg^{2+} and Na^{+} around BWYV pseudoknot (E,I,M,Q), 58-nt rRNA fragment (F,J,N,R), yeast $tRNA^{Phe}$ (G,K,O,S) and SAM-I riboswitch (H,L,P,T) were displayed in green of three-level opacities (0.5 M-5 M, 5 M-10 M and >10 M for Mg^{2+} and 0.25 M-0.5 M, 0.5 M-2.0 M, >2.0 M for Na^{+}) by VMD (11). In panels A-D, the names of helical stems, loops and junctions are corresponding to those in the secondary structures in Fig. S10 in the Supporting Materials. The view of the panels in the opposite direction can be found in Fig. 7 in the main text.

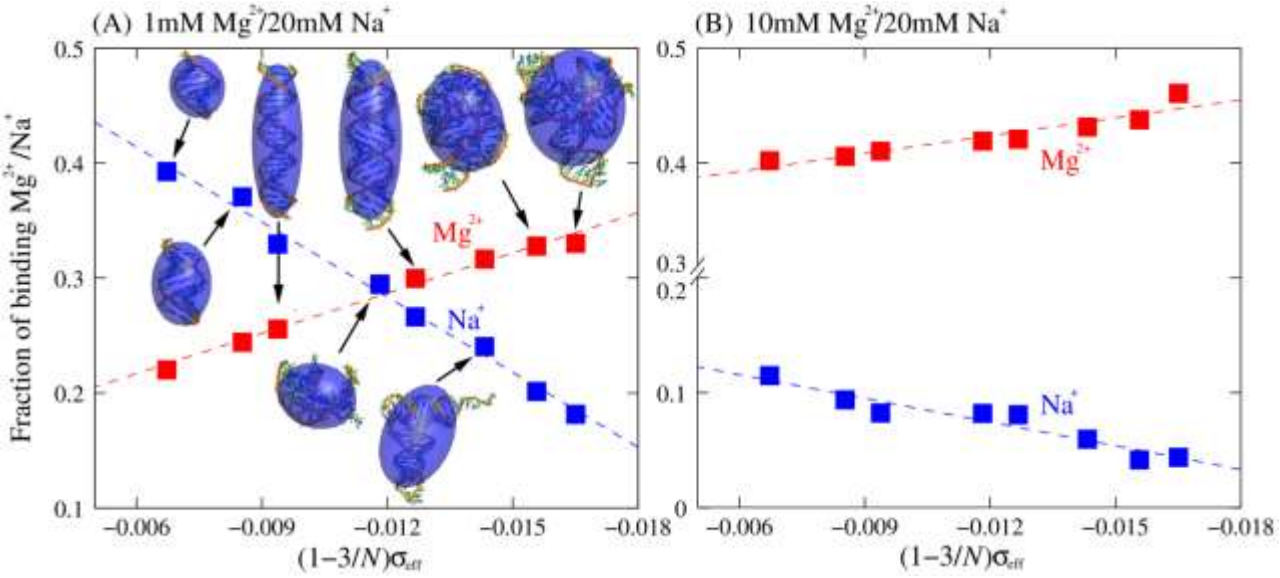

Figure S12 (A,B) The number fractions of binding Mg^{2+} and Na^{+} per nucleotide for various RNA/DNA molecules in mixed 1 mM Mg^{2+}/20 mM Na^{+} (A) and 10 mM Mg^{2+}/20 mM Na^{+} (B) ion solutions. Squares: MD simulations. Here, RNA/DNA molecules were listed according to the value of $(1\text{-}3/N)\sigma_{eff}$. The ellipsoids obtained by Eq. S1 to mimic the shapes of RNA/DNA molecules are displayed with Pymol (http://www.pymol.org).

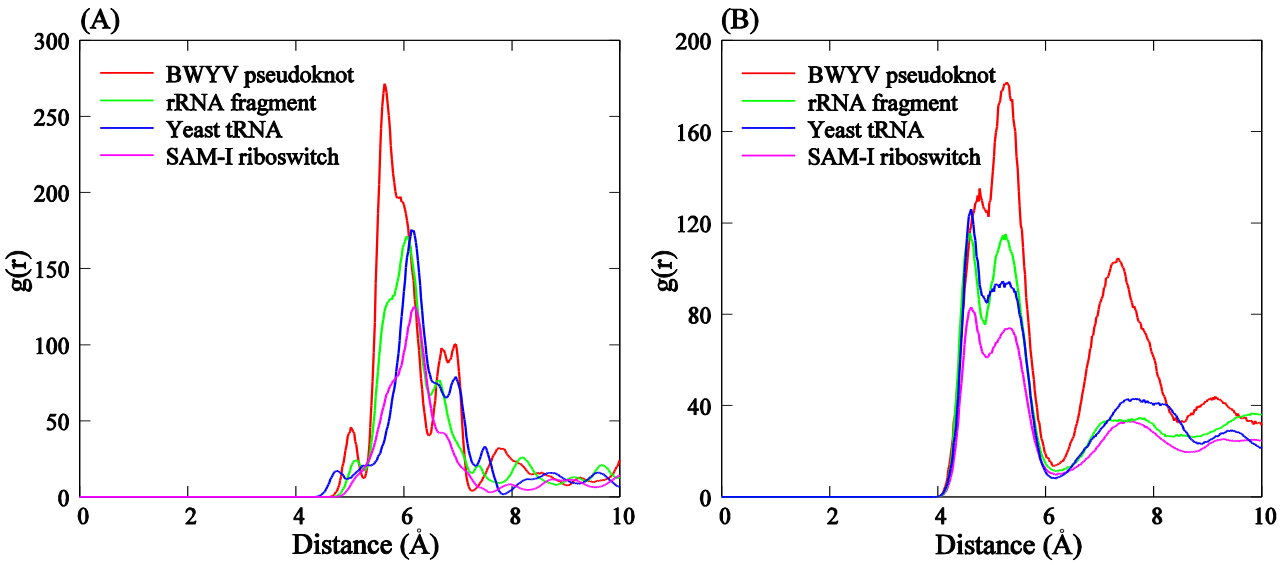

Figure S13 (A) The radial distribution function g(r) of phosphates for various RNA tertiary structures; (B) The radial distribution function g(r) of Mg^{2+} around phosphates for various RNA tertiary structures in mixed 1 mM Mg^{2+}/20 mM Na^{+} solution.

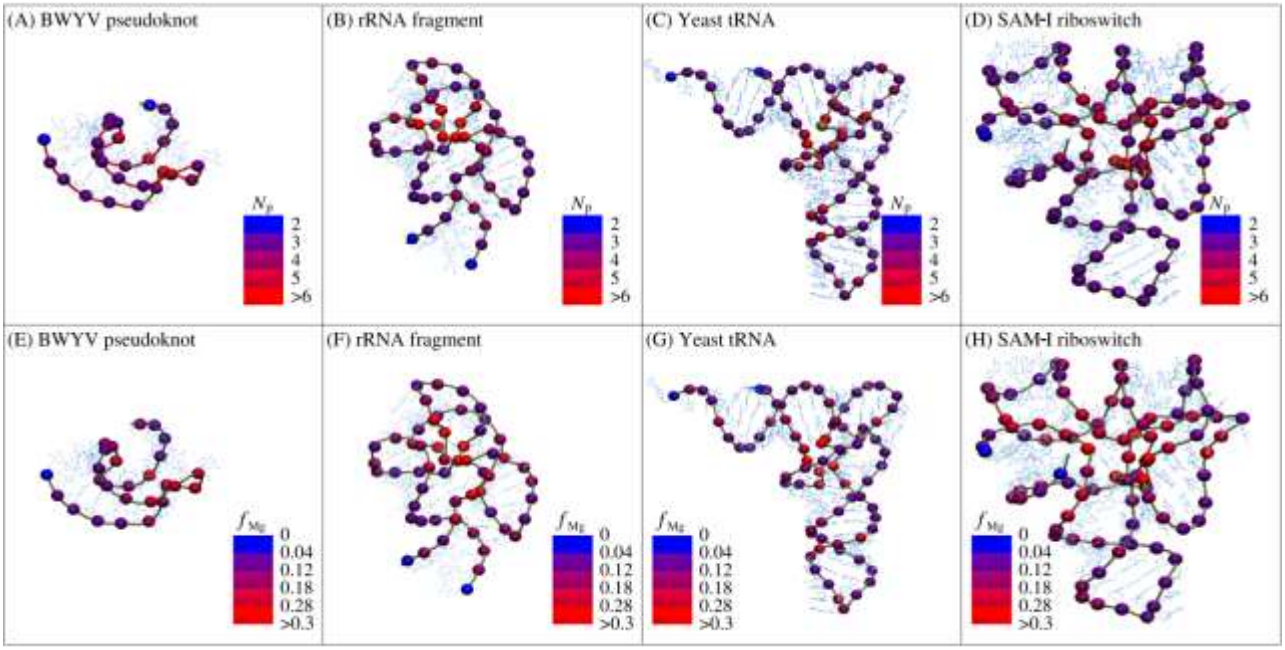

Figure S14 (A-D) The distribution of local phosphate number N_p along phosphate strand for various RNA tertiary structures, and N_p for a phosphate denotes the numbers of phosphates within a distance of 9 Å around the phosphate. (E-H) The distribution of closely binding Mg^{2+} f_{Mg} per phosphate along phosphates strand for various RNA tertiary structures and closely binding Mg^{2+} f_{Mg} for a phosphate denotes the number of Mg^{2+} ions around a phosphate within a distance of 5 Å. The cut-off distances for N_p and for closely binding Mg^{2+}/Na^+ were selected according to the radial distributions of phosphates and Mg^{2+} around phosphates: the range of 9 Å for N_p generally includes next nearest neighbor phosphates and the range of 5 Å for phosphate-Mg^{2+} only includes the nearest closely binding Mg^{2+}/Na^+ (see Fig. S13 in the Supporting Materials). The change of cut-off distance from 5 Å to 6 Å for phosphate-Mg^{2+} does not significantly change the curves of average number fraction of closely binding Mg^{2+} and N_p (see Fig. S15 in the Supporting Materials).

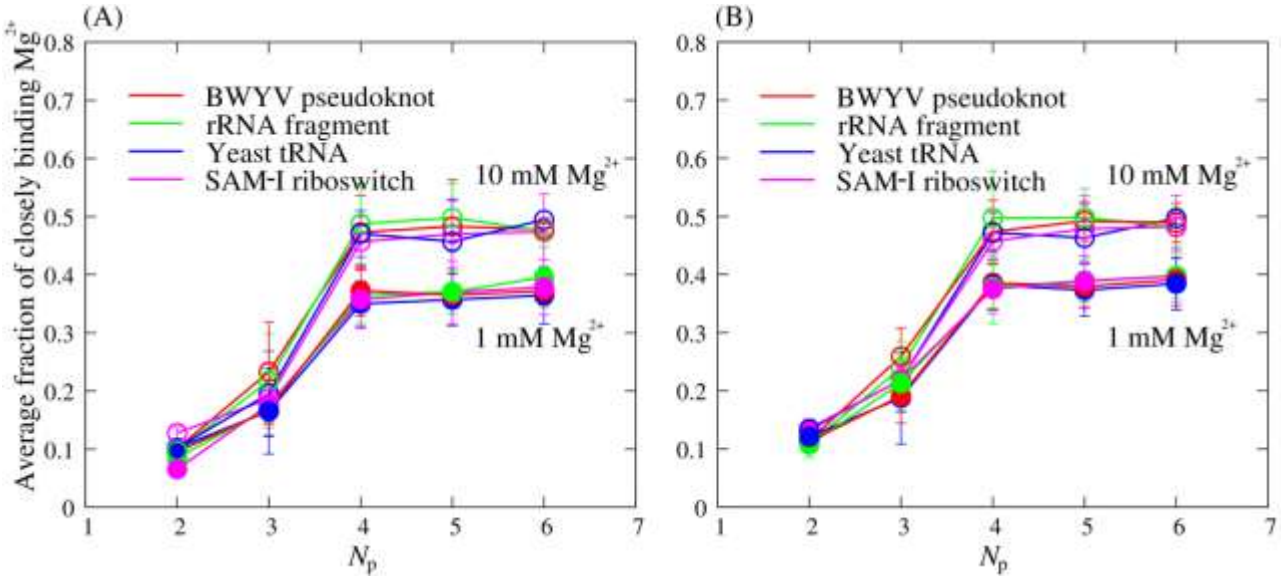

Figure S15 (A,B) The average number fraction of closely binding Mg^{2+} around phosphates within a cut-off distance of 5.5 Å (A) and 6 Å (B) for RNA tertiary structures in 1mM Mg^{2+}/20 mM Na^{+} and 10 mM Mg^{2+}/20 mM Na^{+} solutions, respectively. Larger cut-off distance corresponds to larger numbers of "defined" closely binding ions and smaller saturation point (N_p), which is attributed to more easiness for becoming closely binding ions.

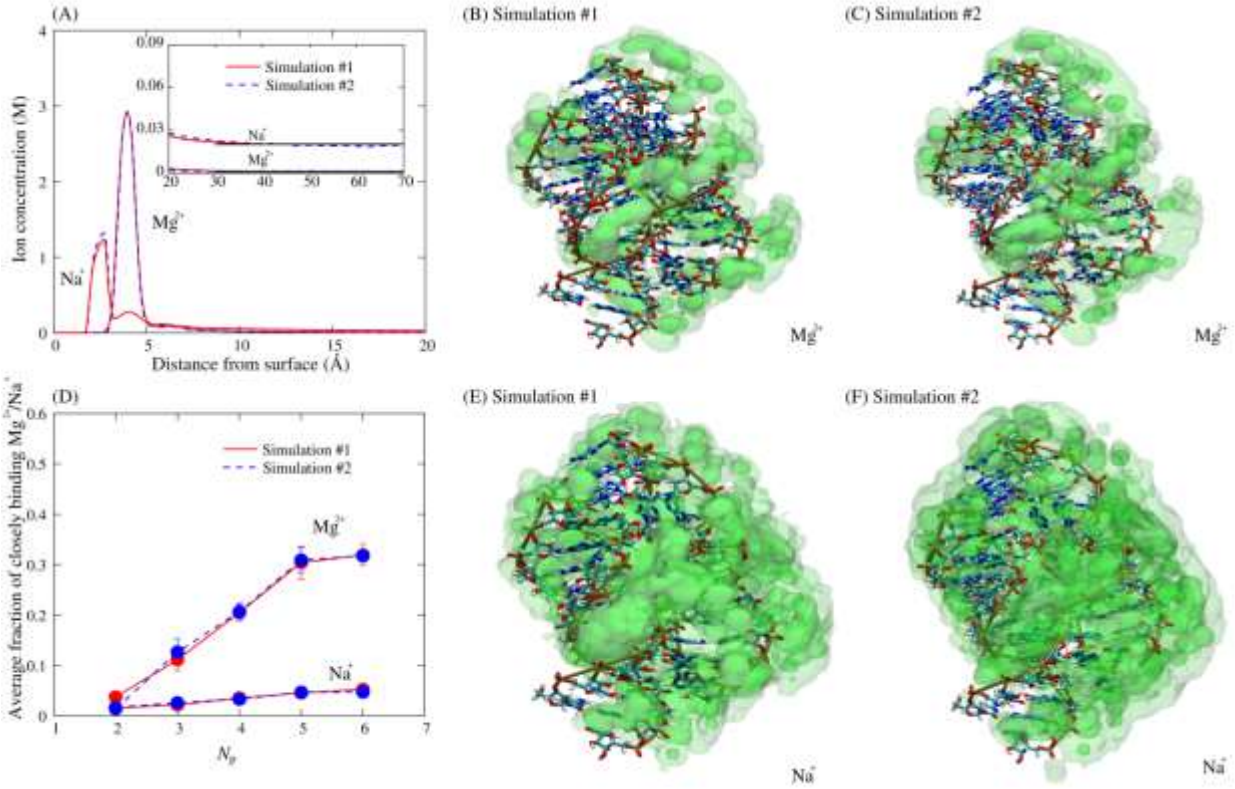

Figure S16 (A) The concentration distribution of Mg^{2+} and Na^{+} around 58-nt rRNA fragment in 1 mM Mg^{2+}/20 mM Na^{+} for the original simulation (simulation #1) and the additional simulation with different initial ions positions (simulation #2). (B,C,E,F) The spatial ion concentration of Mg^{2+} and Na^{+} around 58-nt rRNA fragment for the two simulations with different initial ions positions were displayed in green of three-level opacities (0.5 M-5 M, 5 M-10 M and >10 M for Mg^{2+} and 0.25 M-0.5 M, 0.5 M-2.0 M, >2.0 M for Na^{+}) by VMD (11): simulation #1 (B,E) and simulation #2 (C,F). (D) Average number fraction of closely binding Mg^{2+}/Na^{+} around phosphates within a cut-off distance of 5.0 Å from the two simulations for 58-nt rRNA fragment in 1mM Mg^{2+}/20 mM Na^{+} solutions, respectively.

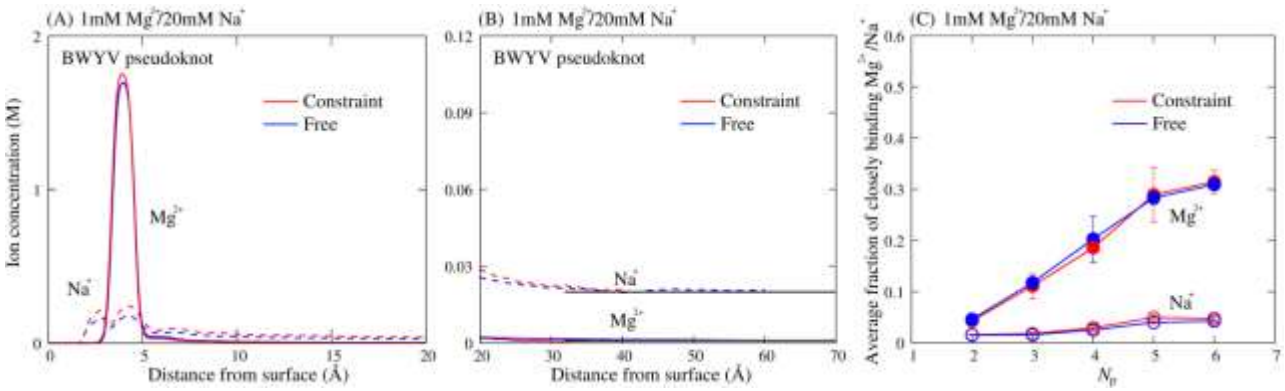

Figure S17 (A,B) The concentration distribution of Mg^{2+} and Na^{+} around 28-nt BWYV pseudoknot in 1 mM Mg^{2+}/20 mM Na^{+} for the original simulation (labeled as constraint) and the additional simulation without constraint (labeled as free). (C) Average number fraction of closely binding Mg^{2+}/Na^{+} around phosphates within a cut-off distance of 5.0 Å from the two simulations for 28-nt BWYV pseudoknot in 1mM Mg^{2+}/20 mM Na^{+} solutions, respectively.

References

1. Manning, G. S. 2007. Counterion condensation on charged spheres, cylinders, and planes. *J. Phys. Chem. B.* 111:8554–8559.
2. Gueron, M. and Weisbuch, G. 1980. Polyelectrolyte theory. I. Counterion accumulation, site-binding, and their insensitivity to polyelectrolyte shape in solutions containing finite salt concentrations. *Biopolymers.* 19:353–382.
3. Bai, Y., Greenfeld, M., Travers, K. J., Chu, V. B., Lipfert, J., Doniach, S. and Herschlag, D. 2007. Quantitative and comprehensive decomposition of the ion atmosphere around nucleic acids. *J. Am. Chem. Soc.* 129:14981–14988.
4. Yoo, J. and Aksimentiev. A. 2012. Improved parametrization of Li^+, Na^+, K^+, and Mg^{2+} ions for all-atom molecular dynamics simulations of nucleic acid systems. *J. Phys. Chem. Lett.* 3:45–50.
5. Åqvist, J. 1990. Ion-water interaction potentials derived from free energy pertubation simulations. *J. Phys. Chem.* 94:8021–8024.
6. Allnér, O., Nilsson, L. and Villa, A. 2012. Magnesium ion-water coordination and exchange in biomolecular simulations. *J. Chem. Theory Comput.* 8:1493–1502.
7. Li, P. F. and Jr., Merz, K. M. 2014. Taking into account the ion-induced dipole interaction in the nonbonded model of ions. *J. Chem. Theory Comput.* 10:289–297.
8. Robbins, T. J., Ziebarth, J. D. and Wang, Y. M. 2014. Comparison of monovalent and divalent ion distributions around a DNA duplex with molecular dynamics simulation and a Poisson-Boltzmann approach. *Biopolymers.* 101:834–848.
9. Li, W. F., Nordenskiöld, L. and Mu, Y. G. 2011. Sequence-specific Mg^{2+}-DNA interactions: a molecular dynamics simulation study. *J. Phys. Chem. B.* 115:14713–14720.
10. Baker, N. A., Sept, D., Joseph, S., Holst, M. J. and McCammon, J. A. 2001. Electrostatics of nanosystems: application to microtubules and the ribosome. *Proc. Natl. Acad. Sci. USA.* 98:10037–10041.
11. Humphrey, W., Dalke, A. and Schulten, K. 1996. VMD: visual molecular dynamics. *J. Mol. Graph.* 14:33–38.
12. Zhang, Z. L., Wu, Y. Y., Xi, K., Sang, J. P. and Tan, Z. J. 2017. Divalent ion-mediated DNA-DNA interactions: a comparative study of triplex and duplex. *Biophys. J.* 113:517–528.